Article

Current Biology

Species-specific spectral tuning of motion vision in butterflies

Graphical abstract

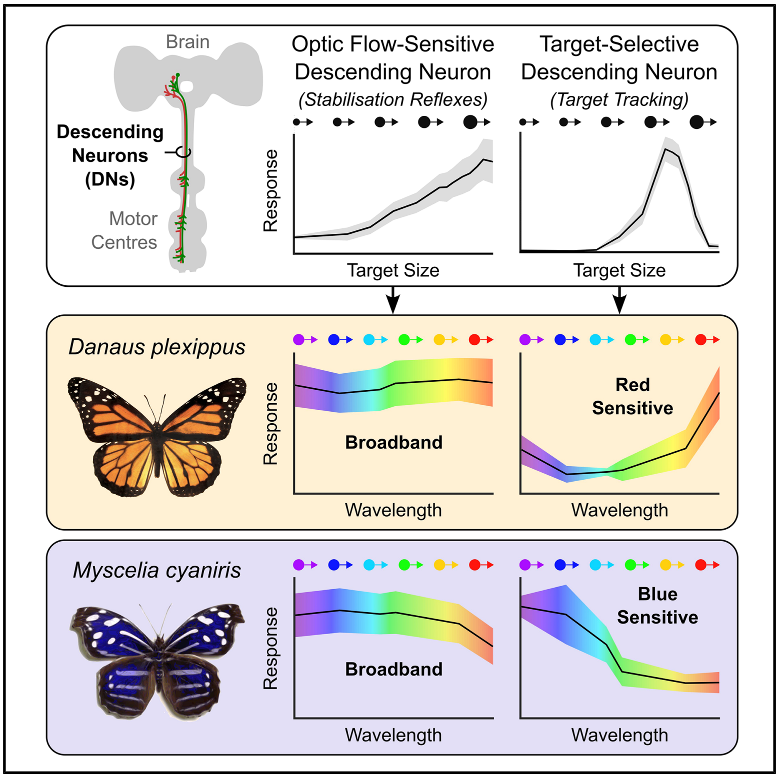

Highlights

- Butterflies are remarkable for their diverse wing coloration and retinal composition
- Parallel motion-sensitive descending neurons (DNs) have different spectral tuning
- Optic flow-sensitive DNs are spectrally broadband, aligning with optomotor responses
- Target-selective DNs are spectrally narrowband and match conspecific wing coloration

Authors

Jack A. Supple, Uroš Cerkvenik, Marko Ilić, Primož Pirih, Aleš Škorjanc, Gregor Belušič, Holger G. Krapp

Correspondence

jackalexsupple@gmail.com

In brief

Supple et al. investigate the spectral sensitivity of motion-sensitive descending neurons (DNs) connecting the brain to thoracic motor centers in butterflies. Optic flow-sensitive DNs are spectrally broadband, corresponding to retinal composition and optomotor reflexes. However, target-selective DNs are spectrally narrowband and spectrally tuned to species-specific wing coloration.

Supple et al., 2026, Current Biology *36*, 290–306
January 19, 2026
https://doi.org/10.1016/j.cub.2025.11.037

CellPress

CellPress
OPEN ACCESS

Current Biology

Article

Species-specific spectral tuning of motion vision in butterflies

Jack A. Supple,[1,4,*] Uroš Cerkvenik,[2] Marko Ilić,[2] Primož Pirih,[3] Aleš Škorjanc,[2] Gregor Belušič,[2] and Holger G. Krapp[1]
[1]Department of Bioengineering, Imperial College London, Exhibition Road, London SW7 2AZ, UK
[2]University of Ljubljana, Biotechnical Faculty, Department of Biology, Večna pot 111, 1000 Ljubljana, Slovenia
[3]Department for Chemistry and Physics of Materials, University of Salzburg, Jakob-Haringer-Str. 2a, 5020 Salzburg, Austria
[4]Lead contact
*Correspondence: jackalexsupple@gmail.com
https://doi.org/10.1016/j.cub.2025.11.037

SUMMARY

Color provides an important visual dimension for object detection and classification. In most animals, color and motion vision are largely separated throughout early stages of visual processing. However, accumulating evidence indicates crosstalk between chromatic and achromatic pathways. Here, we investigate the spectral sensitivity of the motion-vision pathway at the level of pre-motor descending neurons (DNs) in two butterfly species with different retinal compositions and wing coloration. Butterflies engage in fast, agile flight within often colorful visual ecologies, which may heighten evolutionary pressure to integrate color and motion vision. Indeed, we observed a separation of spectral sensitivities that matches the functional properties of butterfly DNs, such that wide-field, optic flow-sensitive DNs involved in stabilization reflexes have effective broadband spectral responses, while target-selective DNs involved in target tracking are comparatively narrowband and match conspecific wing coloration. Our findings demonstrate the spectral tuning of motion vision within a pre-motor neuronal bottleneck that controls behavior.

INTRODUCTION

With less than ~10^6 neurons[1–3] and power consumption in the milliwatt range,[4,5] insects engage with diverse,[6] often agile behaviors,[7,8] far outperforming modern artificial systems.[9] A foundational principle enabling such high-performance information processing is "matched filtering," whereby sensorimotor systems are specialized to process only task-relevant information.[10–13] Indeed, neurons throughout the insect nervous system are highly task-specialized,[11,13,14] with mounting evidence that the insect sensorimotor pathway is matched to maximize signal energy transfer from actuators to sensors.[15–17] Matched filters are prominent throughout insect visuomotor pathways, ranging from specializations for visual acuity[11] to spatial gradients of photoreceptor spectral sensitivities[18] to optic flow-sensitive interneurons that monitor self-motion.[12,16] However, while spectral information provides an important dimension for visual feature extraction,[19] few examples[20] exist in which color vision and motion vision are integrated into matched filters spanning both visual dimensions.

Color and motion vision are conspicuously segregated into parallel anatomical pathways in both vertebrates[21] and invertebrates.[22] In flies, broadband-sensitive photoreceptors R1-6 synapse with lamina monopolar cells (LMCs),[23–25] which are specialized input channels to downstream motion-detecting neurons.[26] In contrast, photoreceptors R7-8 have differential opsin expression and project long visual fibers bypassing the lamina before terminating in the medulla.[25,27] Optic lobe output interneurons separate into distinct anatomical tracts,[22,27] with predominantly achromatic neurons projecting to the lateral protocerebrum and chromatic neurons projecting to the anterior protocerebrum.[22,28] This separation of parallel chromatic/achromatic pathways is thought to arise from the trade-off between spectral acuity and spatiotemporal acuity, with achromatic vision increasing photon capture, thereby improving sensitivity and spatiotemporal resolution.[29,30] Indeed, color vision in bees depends on object size, with recognition of small objects depending predominantly on achromatic luminance contrasts, while chromatic information is exclusively used for larger objects.[31] Nonetheless, examples of crosstalk between chromatic and achromatic pathways are emerging.[20,32–35] For example, asymmetric spectral sensitivities of ON/OFF motion-sensitive T4/T5 cells (the first stage of motion detection[36]) in *Drosophila* enhance the detection of approaching colored objects, demonstrating potential advantages of integrated chromatic motion vision.[20]

Descending neurons (DNs) occupy a focal point in the insect nervous system by connecting the brain to thoracic motor centers.[37,38] As an information bottleneck, DNs integrate sensory modalities to improve the speed and precision of sensorimotor control,[39,40] and subpopulations of specialized DNs are matched to control specific aspects of behavior.[38] Notably, stabilization reflexes and goal-directed behaviors such as target tracking are largely designated to separate DN populations,[41] enabling specialization for the different dynamics of each task.[42] DNs sensitive to wide-field optic flow (WFDNs) have been described in a variety of insects,[43–55] and they respond selectively to a preferred pattern of wide-field motion across a large visual area.[43] WFDNs receive input from optic flow-sensitive output neurons from the optic lobe, project from the lateral protocerebrum to the thoracic ganglia, and are thought to coordinate optomotor stabilization reflexes.[43,44,54,56,57] In contrast, target-selective DNs (TSDNs) are sensitive to small objects moving in a preferred direction,[41,47,50,58] featuring localized receptive fields aligned with other neuroanatomical specializations for target tracking such as increased sensitivity and spatiotemporal acuity.[11,59,60] For example, TSDNs in predatory Odonates and Dipterans align with visual acute zones upon which prey is fixated during interception,[40,59–63] while TSDNs in non-predatory Dipterans sample from the "love-spot"[64] acute zone to track conspecifics.[47,65,66] TSDNs are thought to receive input from small target movement detector interneurons projecting from the lobula complex[67,68] and/or medulla,[65,69,70] and they descend to innervate thoracic motor centers,[47,60,65] often directly synapsing with motor neurons.[47,63,65]

As a sensorimotor interface, DNs present an interesting stage at which to investigate the integration of color and motion vision. Both WFDNs and TSDNs respond to visual inputs, even in immobilized animals,[47,50,51] suggesting that additional dendritic gating mechanisms and/or parallel pathways of DNs are integrated to coordinate behavior.[63] It is presently unknown whether motion-sensitive DNs are achromatic and gated by chromatic information depending on behavioral context or whether motion-sensitive DNs are inherently spectrally selective. In dragonflies, TSDNs are UV/blue sensitive,[71] matching the spectral sensitivity of the dorsal retina.[72,73] However, dragonflies contrast prey silhouettes against the sky by hunting from below,[74–76] so this short-wavelength specialization increases the signal-to-noise ratio of extremely small (<1°) targets.[74,77,78] Similarly, WFDNs[53,71,79] and their inputs from the lobula complex[80–83] are driven primarily by green-sensitive photoreceptors in most tested insects, matching the spectral sensitivity of optomotor behaviors.[82–95] Optomotor green sensitivity is presumed to improve photon catch by matching the predominantly green diurnal terrestrial background,[92,95] with optomotor responses of crepuscular species correspondingly blue-shifted.[95] Additional photoreceptor inputs nonetheless improve wide-field motion detection in flies[32] and bees[79] by increasing photon catch across the visible spectrum.[32]

We investigated the spectral sensitivity of motion vision at the level of DNs in butterflies, a diverse clade[96] remarkable for both their highly maneuverable flight[97] and their often colorful visual ecologies.[98] Butterflies frequently engage in fast aerial pursuits during both courtship and territorial conflicts.[99–102] Males competing for territory execute fast spiraling flights, with both males sequentially exchanging status as chaser and evader until one concedes.[99,102–105] Similarly, courtship in many species is initiated by males pursuing flying conspecific females.[100,105–107] Both sexes broadly assess mate quality from multiple cues including color,[108–111] size,[109,111] and odor,[108–110] with females suggested to use aerial pursuit to identify fitter mates.[111,112] The flight performance demanded by sexual behaviors necessitates a combination of robust stabilization reflexes functioning in parallel with a specialized target-tracking system.[14,42,113–115] The ubiquitous use of color throughout butterfly behavioral ecology may impose selective evolutionary pressures to integrate color and motion vision. Indeed, butterfly wide-field motion vision is sensitive to chromatic-only contrasts,[35] unlike in flies[94] and bees.[87]

Butterfly color vision is supported by nine photoreceptors R1–9 per ommatidium, forming a fused and tiered rhabdom,[116] with diverse patterns of opsin and pigment expression across the retina depending on species.[117] R1&2 project long visual fibers (LVFs) to the medulla, while R3–8 are short visual fibers (SVFs), terminating in the lamina.[118,119] Basal R9 forms a LVF[119,120] or SVF[118] depending on species. Inter-photoreceptor synapses produce additional combinations of spectral opponency,[118,121] and an array of spectrally narrowband interneurons span from 300–650 nm in the mushroom bodies.[122–124] While most LMCs are spectrally broadband, receiving multiple photoreceptor inputs,[95,118,125] some heterogeneity between LMC types suggests the potential for spectrally selective motion vision.[125] Indeed, one early study reported species-dependent spectral selectivity in butterfly WFDNs,[53] and motion-sensitive feedback neurons projecting from the protocerebrum to the medulla are sensitive to chromatic-only contrasts.[34] In this study, we report the functional properties of a subset of butterfly motion-sensitive DNs, finding WFDNs and TSDNs akin to those reported in other species. We then compared DN spectral sensitivities, finding a functional separation whereby WFDNs have effective broadband spectral responses matching optomotor reflexes, while TSDNs are comparatively narrowband and match conspecific wing coloration.

RESULTS

Diversity of butterfly wing coloration and retinal composition

We compare two species of New World Nymphalid butterflies: the Monarch butterfly *Danaus plexippus* and the Blue-wave butterfly *Myscelia cyaniris* (referred to hereon by their genus). With a last common ancestor ∼78.85 mya,[96] *Danaus* and *Myscelia* have notable divergence in wing coloration (Figure 1A). *Danaus* are aposematic, signaling their toxicity to predators via a distinctively bright-orange wing coloration[126,127] (Figure 1Ai). Reflectance increases between 500–700 nm (Figure 1Bi). While coloration is slightly red-shifted in males and migration-stage butterflies,[128] sexual dimorphism is minimal, limited to enlarged black vein widths in females and two black androchonial pheromone glands on the male hindwings (Figure 1Ai). *Myscelia* sexual dimorphism is more pronounced (Figure 1Aii). Both sexes are striated with light bands across both wings (Figure 1Aii). However, males possess a vibrant blue iridescence, with a reflectance maximum at ∼370 nm and half-max at 460 nm (Figure 1Bii). This coloration is largely absent in females, although the light stripes possess a subtle shade of violet (Figure 1Aii).

Danaus and *Myscelia* are also divergent in their retinal composition (Figure 1C). Previous work demonstrated that Nymphalid photoreceptor rhodopsin expression patterns produce either simple or complex retina types depending on sex and species.[121,129] The basic (simple) composition of Nymphalid retinas includes SVF R3–8 expressing long-wavelength, green- or yellow-peaking rhodopsins, while LVF R1&2 express either UV or blue-peaking rhodopsins.[121,129] *Myscelia* retinas correspond to this simple design, with three photoreceptor types peaking in UV, blue, and green (Figure 1Cii), with inhibitory green opponency in UV and blue photoreceptors (U^+G^- and B^+G^-, respectively). Complex retinas contain all ommatidial types found in

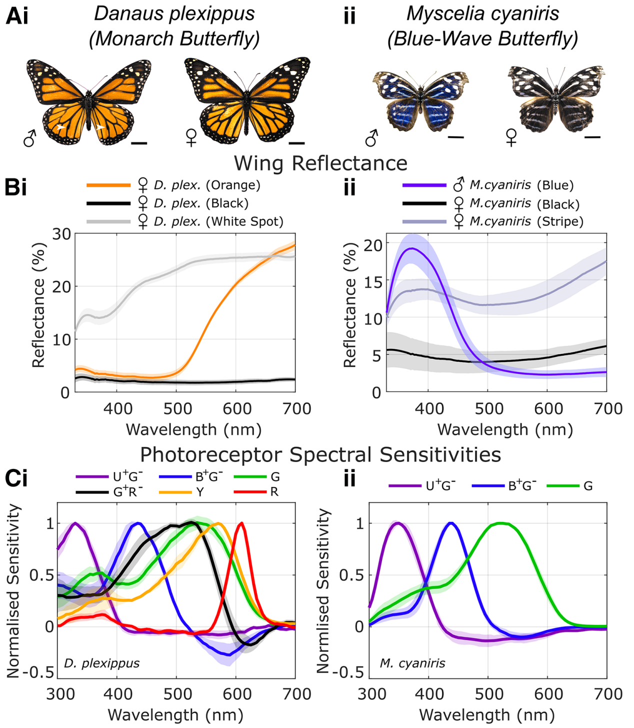

Figure 1. Photoreceptor spectral sensitivities and wing coloration in *D. plexippus* and *M. cyaniris*

(A) Male and female specimens of (i) *D. plexippus* and (ii) *M. cyaniris*. Scale bars, 1 cm. All specimens displayed at the same scale for comparison. Hindwing androconial scent glands indicated by white arrowheads for male *D. plexippus*.

See also Video S3.

(B) Wing reflectance measurements (mean ± SEM). (i) *D. plexippus* forewing reflectance from orange and black perimeter regions, and white spots. $N = 2$ animals. (ii) *M. cyaniris* reflectance from male blue forewing ($N = 3$ animals), female black regions (combined fore- and hindwings, $N = 2$ animals), and female white/violet stripes (combined fore- and hindwings, $N = 2$ animals).

(C) Photoreceptor spectral sensitivities from (i) *D. plexippus* ($N = 4/5/8/3/6/2$, $U^+G^-/B^+G^-/G/G^+R^-/Y/R$ cells from 4 animals) and (ii) *M. cyaniris* ($N = 4/4/7$, $U^+G^-/B^+G^-/G$ cells from 2 animals). Data show mean ± SEM.

simple retinas; however, an additional ommatidial type expresses a long-wavelength (green) rhodopsin in R1&2.[129–131] These ommatidia also contain a red screening pigment that filters light reaching the photoreceptors at the base of the retina; the proximal R5–8 are therefore yellow shifted (termed "Y" receptors), while the basal R9 is red sensitive.[129,131] Inhibitory synapses between red-sensitive R9 and green R1&2 produce green-red opponent (G^+R^-) cells.[131] The retina of *Danaus* corresponds to this complex form, with red-sensitive R9, yellow-sensitive R5–8, and G^+R^- extending spectral sensitivity to 650 nm (Figure 1Ci).

Parallel pathways of motion-sensitive DNs in butterflies

To investigate the spectral sensitivity of butterfly DNs, we presented moving patterns in the frontal visual field using a customized display system comprising a multi-LED 2D-galvanometer (galvo) scanner and an RGB digital light processing (DLP) projector (Figure S1A). Using the DLP, we first classified DNs into two functional categories based on their sensitivity to different moving patterns. WFDNs (Figure 2) were classified as neurons with (1) directionally selective responses to wide-field moving gratings with approximately cosine tuning curves and (2) monotonically increasing responses to increasing target sizes. TSDNs (Figure 5) were classified as neurons that (1) displayed non-linear target-size tuning curves with a single distinct peak,[50] (2) responded to targets with a distinct preferred direction of motion, and (3) responded weakly (<20 spikes/s) to wide-field moving gratings. We subsequently measured DN spectral tuning curves, using the multi-LED galvo scanner, which presented moving bright objects subtending 8° diameter (Figure S1A).

WFDNs are spectrally broadband and reflect retinal composition

In both species, the most frequently encountered WFDN was sensitive to horizontal motion ($WFDN_H$; Figure 2), with a baseline spontaneous firing rate of 8.1 ± 6.1 and 7.1 ± 6.0 spikes/s (mean ± SEM; *Danaus* and *Myscelia*, respectively), increasing to a maximum of 38.8 ± 8.7 and 38.1 ± 6.5 spikes/s in the preferred direction (toward the ipsilateral side) and decreasing to 1.6 ± 0.47 and 1.4 ± 0.6 spikes/s in the anti-preferred direction (*Danaus*: $N = 7$ units, 6 animals; *Myscelia*: $N = 8$ units, 5 animals; Figures 2Di–2Ei). $WFDN_H$ receptive fields were binocular in both species (Figures 2Diii and Eiii), although *Myscelia* $WFDN_H$ was more lateralized to the ipsilateral visual field (Figure 2Eiii).

$WFDN_H$ spectral sensitivities were broadband in both species (Figures 2Div and 2Eiv). However, *Danaus* $WFDN_H$ displayed a subtle reduction in blue sensitivity (reduction of normalized mean spike rate by −7%; ANOVA $p = 0.02$; t test comparison to average, $p = 0.04/p > 0.05$ before/after Bonferroni correction for multiple comparisons; Figure 2Div), while *Myscelia* $WFDN_H$ had a more pronounced reduction in sensitivity for red objects (reduction of normalized mean spike rate by −38%; ANOVA $p < 10^{-7}$; t test comparison to average, $p < 10^{-3}$ with Bonferroni correction; Figure 2Eiv). *Myscelia* $WFDN_H$ responses were well explained by green photoreceptor input (corresponding to SVFs R3–8; $R^2 = 0.70$; Figure 2G), with additional B^+G^- receptor input improving the modeled response ($R^2 = 0.85$; green:blue = 1:0.37; Figures 2Giii and 2Giv). *Myscelia* $WFDN_H$ responses were also compatible with inputs weighted according to the anatomical distribution of photoreceptors in the retina (U^+G^-:B^+G^-:G = 2:1:9, see STAR Methods; $R^2 = 0.77$; Figure 2Giv). In contrast, *Danaus* $WFDN_H$ spectral sensitivity was poorly modeled by green-only photoreceptor input ($R^2 = -3.3$; Figure 2Fiv) or SVF-only inputs (corresponding to G/Y photoreceptors; $R^2 = -2.0$) but were compatible with a range of multi-photoreceptor input combinations ($R^2 > 0.9$; Figure 2Fiii). Notably, an estimate of anatomical photoreceptor ratios poorly explained *Danaus* $WFDN_H$ responses (U^+G^-:B^+G^-:G:G^+R^-:Y:R = 5:10:45:2:8:2, see STAR Methods; $R^2 = -3.2$; Figure 2Fiv), suggesting differential photoreceptor weighting contributed to WFDN responses.

To further investigate DN spectral sensitivities, we tested spectral responses to an extended sequence of moving patterns using the RGB DLP (Figure 3). In both species, we found no statistically significant differences in $WFDN_H$ preferred-direction response gain to moving gratings with different colors (Figures 3A and 3E; non-parametric permutation tests,

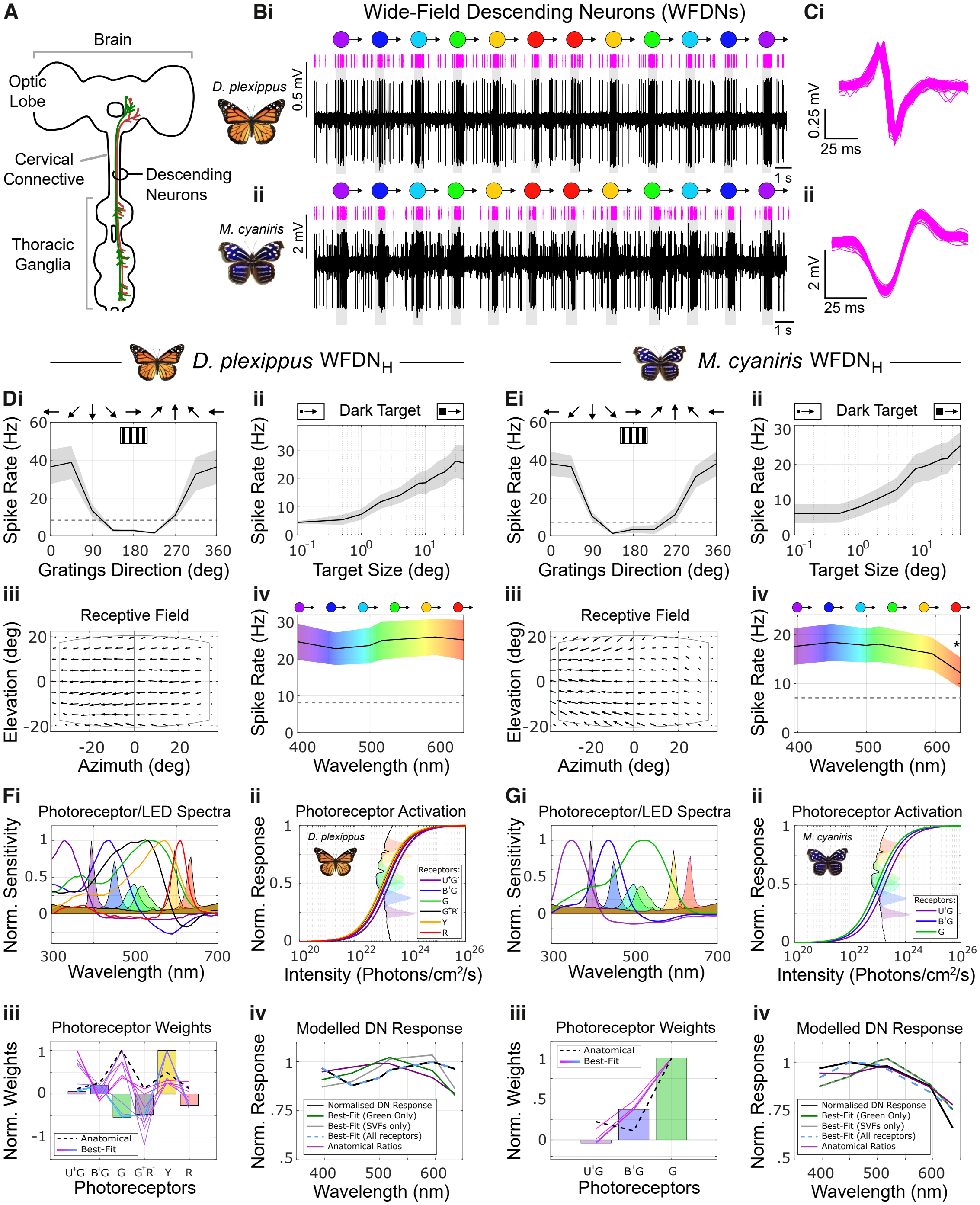

Figure 2. WFDN spectral sensitivities in *D. plexippus* and *M. cyaniris*

(A) Schematic of butterfly nervous system and DNs. DNs were recorded from the cervical connective. Nervous system is viewed from the ventral aspect, with DNs illustrated on the animal's left.

(B) Example raw extracellular voltage traces of WFDNs in (i) *D. plexippus* and (ii) *M. cyaniris* responding to 8°-diameter circular bright objects of different color moving in the preferred direction. Gray regions indicate periods of target movement. Magenta lines show the sorted spikes from each WFDN unit.

(C) Spike-sorted waveforms for the recordings in (B).

(D and E) WFDN$_H$ responses from (D) *D. plexippus* (WFDN$_H$, $N = 7$ units from 6 animals) and (E) *M. cyaniris* (WFDN$_H$, $N = 8$ units from 5 animals). (i) Responses to gratings moving in different directions in the frontal visual field. Dashed gray line shows average spontaneous firing rate. (ii) Responses to dark objects of different side-length subtended angles (degrees) moving in the preferred direction through the receptive field. (iii) DN receptive fields. Vector directions and magnitudes represent the local preferred direction and normalized motion sensitivity of the neuron across the visual field. Positive azimuth/elevation values correspond to the animal's dorsal/right, respectively. (iv) Spectral tuning curves showing DN responses to a bright 8°-diameter circular object moving at a constant velocity of

(legend continued on next page)

$p > 0.05$ after multiple test corrections; Figure S2A). However, when testing a range of temporal frequencies, *Danaus* WFDN_H displayed a subtle response reduction for blue gratings at higher temporal frequencies (Figure 3B; non-parametric permutation tests, $p < 0.05$ after multiple test corrections; $N = 3$ units; Figure S2Bi), whereas *Myscelia* WFDN_H displayed a more prominent reduction to red gratings (Figure 3F; non-parametric permutation tests, $p < 0.05$ after multiple test corrections; $N = 3$ units; Figure S2Bii). There were no statistically significant differences in WFDN_H responses to dark objects of different sizes (Figures 3Ci and 3Gi) or different velocities (Figures 3Di and 3Hi) when moving on a bright background (non-parametric permutation tests, $p > 0.05$ after multiple test corrections, Figures S2C and S2E). However, for bright objects moving on a dark background, there was a subtle reduction in *Danaus* WFDN_H responses for blue targets and a reduction in *Myscelia* WFDN_H responses for red targets, for variations in both target size (Figures 3Cii and 3Gii) and velocity (Figures 3Dii and 3Hii). These response reductions matched those observed for both the multi-LED galvo stimuli (Figures 2Div and 2Eiv) and gratings of variable temporal frequency (Figures 3B and 3F), but they were only statistically significant for *Danaus* WFDN_H after Bonferroni corrections (non-parametric permutation tests, $p < 0.05$, $N = 7$ units, Figures S2D and S2F).

WFDN spectral sensitivities correspond to optomotor behavior

To test whether DN spectral sensitivities match behavior, we measured the spectral sensitivity of stabilizing optomotor head movements in both species (Figure 4). Perched butterflies rotated their head yaw orientation in response to gratings moving horizontally on a spectrally calibrated computer monitor (Videos S1 and S2). Head yaw rotation amplitude was maximal at a grating temporal frequency of ~20 cycles/s in both species (Figures 4B–4D). When tested with differently colored gratings, *Danaus* displayed a reduction in maximal yaw amplitude for blue gratings (Figures 4Di–4E; 7.3 ± 1.6, 8.8 ± 1.2, and 8.4 ± 1.1 degrees, blue/green/red, respectively. $N = 17$ animals. Friedman test, $p < 0.05$, and post hoc pairwise t tests with Bonferroni correction, blue-green: $p = 0.049$; blue-red: $p = 0.018$; green-red: $p > 0.5$). In contrast, *Myscelia* head yaw rotation amplitudes were maximal for green and minimal for red gratings (Figures 4Dii and 4E; 6.6 ± 1.3, 7.1 ± 1.2, and 5.1 ± 1.4 degrees, blue/green/red, respectively. $N = 8$ animals. Friedman test, $p < 0.05$, and post hoc pairwise t tests with Bonferroni correction, blue-green: $p = 0.06$; blue-red: $p = 0.06$; green-red: $p = 0.037$). This reduction in head yaw optomotor amplitude for blue gratings in *Danaus* and red gratings in *Myscelia* follows the same spectral sensitivity trends that we observed for WFDNs (Figures 2 and 3).

Butterfly TSDNs are spectrally narrowband

The most frequently encountered TSDNs in *Danaus* were sensitive to either horizontal or ventral-dorsal target motion (TSDN_H and TSDN_D; Figures 5Ciii and 5Diii; TSDN_H: $N = 11$ units, 9 animals; TSDN_D: $N = 3$ units, 2 animals). The most frequently encountered TSDNs in *Myscelia* were sensitive to either horizontal or dorsal-ventral target motion (TSDN_H and TSDN_V; Figures 5Eiii and 5Fiii; TSDN_H: $N = 5$ units, 4 animals; TSDN_V, $N = 6$ units, 5 animals; note only TSDNs from male *Myscelia* were measured). All TSDNs in both species had negligible spontaneous firing rates (<1 spikes/s), were maximally sensitive to a dark-contrast target size of 8° (Figures 5Cii–5Fii), and had ipsilateral receptive fields (Figures 5Ciii–5Fiii). TSDN responses to moving gratings were absent, except for *Danaus* TSDN_D, which responded to gratings moving in the same preferred direction as for target responses (Figure 5Di), albeit with substantially lower spike rates than WFDN_H (Figures 2Di and 2Ei).

Unlike WFDNs, TSDNs in both species had pronounced narrowband spectral sensitivity (Figures 5Civ–5Fiv). In *Danaus*, TSDN_H and TSDN_D were sensitive maximally to red (636 nm) and minimally to green (499 nm), with a smaller secondary maximum for UV (395 nm; Figures 5Civ and 5Div). In *Myscelia*, TSDN_H and TSDN_V were maximally sensitive to short wavelengths (TSDN_H maximum = 470 nm and TSDN_V maximum = 420 nm, based on smoothened estimates; Figures S5H and S5I) and were minimally sensitive to orange/red (Figures 5Eiv and 5Fiv).

Best-fit linear combinations of photoreceptor inputs to *Danaus* TSDNs indicated primary input from Y-receptor (Figures 5G and 5H) but were also compatible with several different multi-photoreceptor combinations ($R^2 > 0.9$; Figures 5Gi and 5Hi). Notably, like *Danaus* WFDN_H, green-only inputs, SVF-only inputs, or weights derived from estimated anatomical photoreceptor count ratios poorly explained *Danaus* TSDN spectral sensitivity (TSDN_H: $R^2 = -0.2, 0.3, -0.1$; TSDN_D: $R^2 = -0.14, 0.11, -0.11$; green/SVF/anatomical ratios, respectively; Figures 5Gii and 5Hii), suggesting differential photoreceptor weighting and inputs from LVFs. For *Myscelia*, TSDN_H responses were poorly modeled by linear combinations of multi-photoreceptor inputs ($R^2 = 0.5$, Figure 5I), but TSDN_V was compatible with predominantly B^+G^- photoreceptor input ($R^2 = 0.86$; Figure 5J). Like *Danaus*, *Myscelia* TSDNs were poorly modeled by SVF-only (i.e., green) inputs or weights derived from anatomical photoreceptor count ratios

115°/sec. Dashed gray line shows WFDN spontaneous firings rates. WFDN responses are statistically significantly different, as determined from ANOVA ($p < 0.01$) followed by post hoc t test comparisons indicated (*$p < 0.05$). Data show mean ± SEM.

(F and G) Modeled WFDN_H LED-galvo responses from linear combinations of photoreceptor inputs for (F) *D. Plexippus* and (G) *M. cyaniris*. (i) Overlap of photoreceptor spectral sensitivities and normalized isoquantal LED emission spectra. (ii) Log-logistic normalized photoreceptor activation as a function of stimulus light intensity. Filled histograms show the absolute LED emission intensities, corresponding to the LED emission spectra in (i). Black line corresponds to the background intensity to which photoreceptors are assumed to be adapted. (iii) Least-squares best-fit photoreceptor weights that reproduce WFDN_H spectral sensitivity. Bars correspond to the overall best-fit photoreceptor weights. Blue-magenta "best-fit" lines show regularized photoreceptor weight combinations that reproduce DN responses with $R^2 \geq 90\%$ the overall best-fit value; blue-magenta lines correspond to small-large regularization penalties, respectively. Dashed black line shows an estimate of anatomical photoreceptor ratios. (iv) Least-squares best-fit WFDN_H response for (green) green-only input, (gray) SVF-only inputs, (dashed blue) all photoreceptors, and (purple) anatomically informed photoreceptor ratio estimates. Black line shows normalized WFDN_H response measured with the LED-galvo. Note that black and dashed blue curves overlay precisely for *Danaus*.

See also Figure S1.

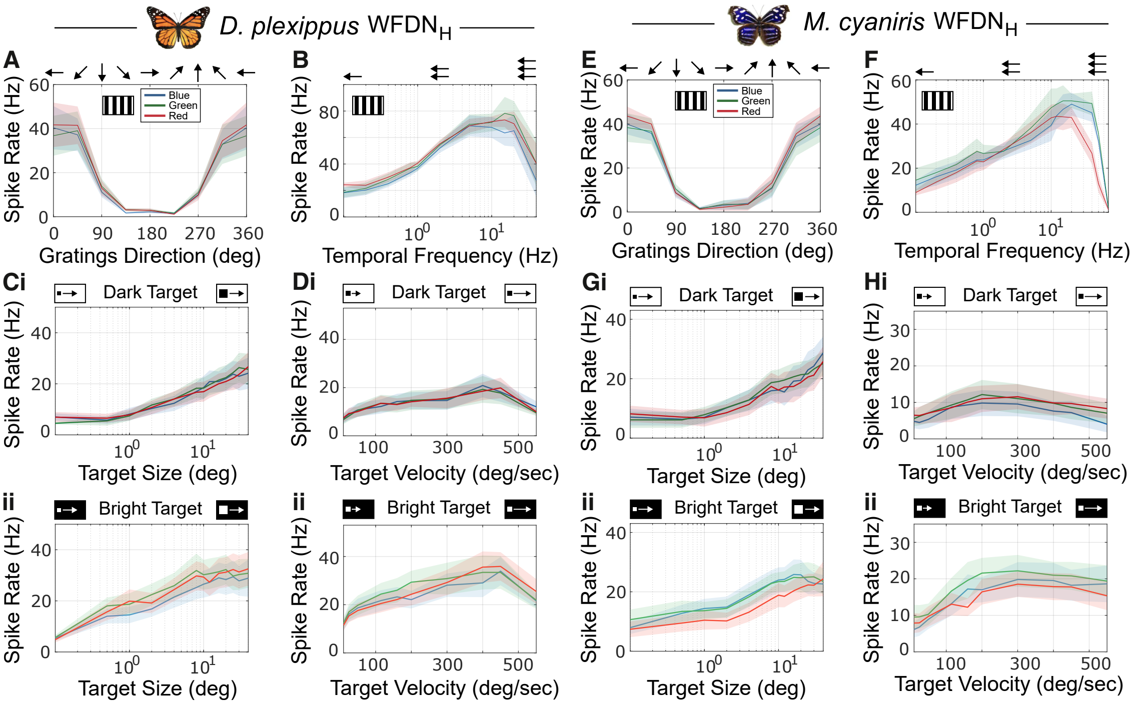

Figure 3. WFDN size and velocity tuning

Extended stimuli for WFDN$_H$ in (A–D) *D. plexippus* and (E–H) *M. cyaniris*. Blue/green/red lines correspond to blue/green/red DLP stimuli. (A and E) WFDN$_H$ responses to gratings moving along different directions in the frontal visual field (10° wavelength, 5 Hz temporal frequency). (B and F) Temporal frequency tuning curves for gratings moving in the preferred direction. (C and G) Size tuning curves for (i) dark and (ii) bright square objects moving in the preferred direction at constant 115°/s velocity. (D and H) Velocity tuning curves for (i) dark and (ii) bright square objects with constant side lengths subtending 4° and moving in the preferred direction. Data show mean ± SEM.

See Figure S2 for statistical analysis. *D. plexippus* (A, C, and D) $N = 7$ units, 6 animals; (B) $N = 3$ units, 3 animals. *M. cyaniris* (E, G, and H) $N = 8$ units from 5 animals; (F) $N = 3$ units, 3 animals.

See also Figure S1.

(TSDN$_H$: $R^2 = 0.29, 0.31$; TSDN$_V$: $R^2 = 0.06, 0.17$; SVF/anatomical ratios, respectively; Figures 5Iii and 5Jii).

While these TSDNs were the most frequently encountered during experiments, other TSDNs were also found less regularly, including TSDN$_V$ in *Danaus*, which displayed similar functional properties to *Myscelia* TSDN$_V$, but shared the UV/red spectral sensitivity of *Danaus* TSDN$_H$ and TSDN$_D$ (Figure S5A). Although we focused on measuring male *Myscelia* TSDNs, we found no difference in TSDN spectral sensitivities between male and female *Danaus* TSDN$_H$ (Figures S5C–S5G).

Unlike WFDN$_H$, TSDNs in both species displayed distinct spectral selectivity across a range of target sizes and velocities (Figure 6). Responses to dark targets moving on a bright background were similar in magnitude for red, green, and blue light, although both species had a slight reduction in responses to blue targets on dark backgrounds for variations in both target size (Figures 6Ai and 6Ci) and velocity (Figures 6Bi and 6Di). Spectral selectivity was more prominent for bright targets moving on a dark background (Figures 6Aii–6Dii), consistent with measurements using the multi-LED galvo system (Figures 5Civ–5Fiv). In *Danaus*, TSDN$_H$ displayed statistically significantly larger peak firing rates for bright red targets (Figures 6Aii and 6Bii; non-parametric permutation tests $p < 0.05$ after multiple test corrections, $N = 10$ units), while *Myscelia* TSDN$_V$ responded more to bright blue targets (Figures 6Cii and 6Dii; non-parametric permutation tests $p < 0.05$ after multiple test corrections, $N = 6$ units). These trends were consistent for variations in both target size (Figures 6Aii and 6Cii) and velocity (Figures 6Bii and 6Dii; Figure S3 for statistical analyses).

Notably, we found that *Danaus* TSDNs responded with highest peak firing rates to bright red targets moving at velocities > 400°/s (Figure 6Bii). These fast-moving bright red targets acted as a super-stimulus, eliciting ∼1.9× the response (maximum of 36.8 ± 18.9 spikes/s at 400°/s), compared with any other tested stimulus parameter (19.7 ± 18.2 spikes/s for bright blue targets at 550°/s; Figure 6Bii). We confirmed that this high-velocity sensitivity was directionally selective (Figure S5B). We also observed substantial differences in TSDN size preference for dark vs. bright moving targets (Figures 6A and 6C). In both species, dark objects produced peak responses for ∼8° target diameters (Figures 6Ai and 6Ci), while bright targets produced peak responses at diameters of ∼1° (Figures 6Aii and 6Cii).

Butterfly TSDN spectral tuning matches conspecific wing reflections under natural skylight

To test whether TSDN spectral sensitivities match target-tracking behaviors, we extended our optomotor head rotation protocol to include bright targets of varying size moving horizontally across

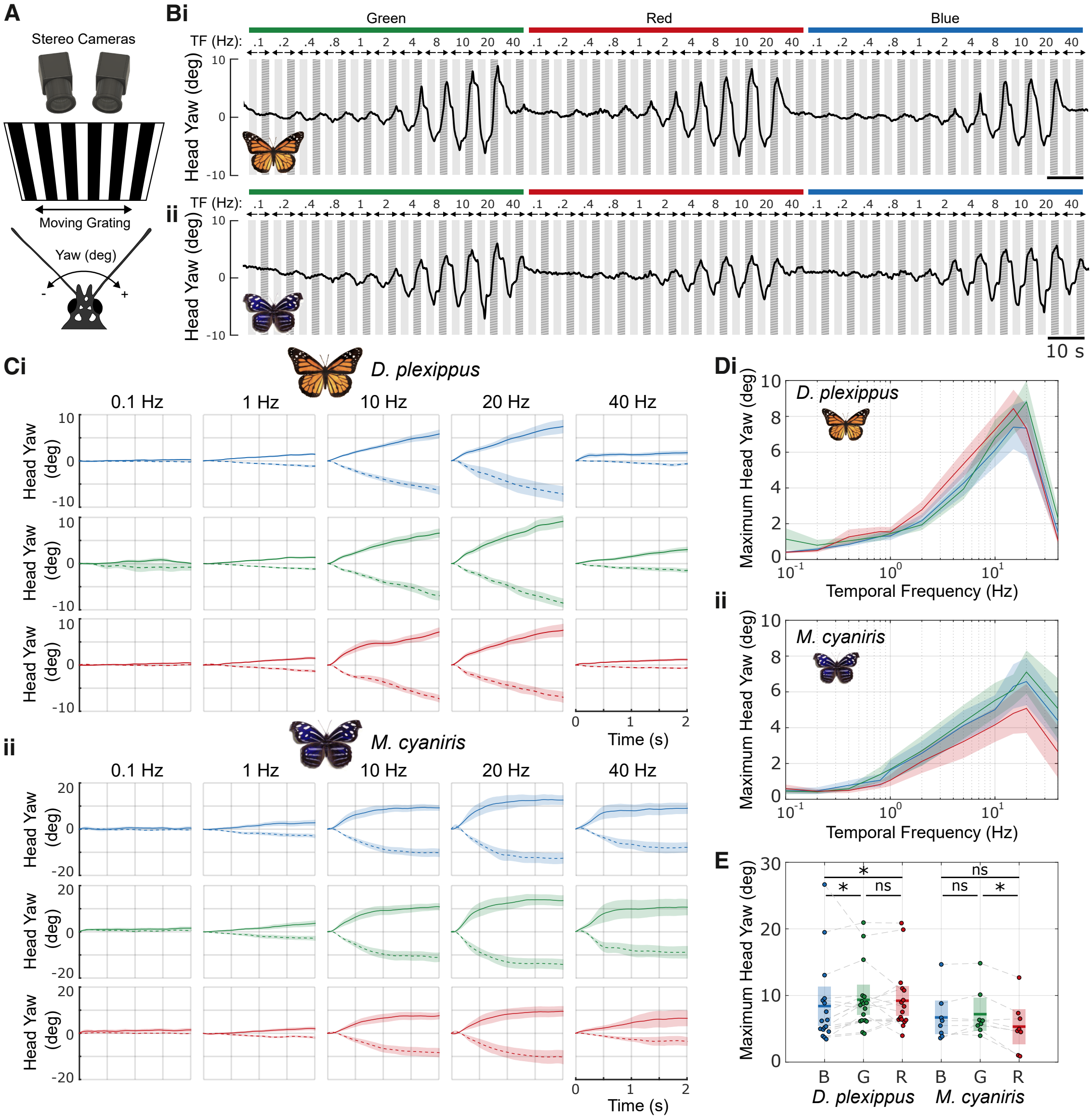

Figure 4. Spectral sensitivity of butterfly optomotor head movements

(A) Perched butterflies rotated their heads in response to gratings (20° spatial wavelength) moving horizontally on a spectrally calibrated computer monitor. 3D head rotations were reconstructed from stereo-videography at 250 fps.
See Videos S1 and S2.
(B) Example head yaw response from (i) *D. plexippus* and (ii) *M. cyaniris* to red, green, or blue gratings moving at temporal frequencies (TFs) ranging from 0.1 to 40 Hz. Gratings moving left and right indicated by light and dark gray periods, respectively.
(C) Time course of head yaw rotations (mean ± SEM) for (i) *D. plexippus* ($N = 17$ animals) and (ii) *M. cyaniris* ($N = 8$ animals). Dashed and solid lines correspond to head responses to gratings moving left (i.e., in the animal's negative yaw direction) and right, respectively. Data displayed relative to head yaw position at grating movement onset. Only 5 of the 11 tested TFs are shown.
(D) Maximum of average left and right head yaw amplitudes for each tested temporal frequency for (i) *D. plexippus* ($N = 17$ animals) and (ii) *M. cyaniris* ($N = 8$ animals). Data show mean ± SEM.
(E) Comparison of peak temporal frequency head yaw amplitudes for each grating color. Peak head yaw responses for different grating colors were statistically significantly different for both *D. plexippus* and *M. cyaniris* (Friedman test, $p \leq 0.05$). Post hoc Bonferroni-corrected pairwise comparisons indicated as * for $p \leq 0.05$. *D. plexippus*: blue-green: $p < 0.05$; blue-red: $p < 0.05$; green-red: $p > 0.5$. *M. cyaniris*: blue-green: $p > 0.5$; blue-red: $p > 0.5$; green-red: $p = 0.04$. Data show mean ± SEM.
See also Figure S4.

the screen (Figure S4). We did not observe any head rotations to moving targets in *Myscelia*; however, *Danaus* occasionally rotated their heads to follow target movement (Figure S4A). While there was a subtle increase in head yaw response amplitudes for red targets and a reduction for small blue targets, this trend was statistically insignificant after accounting for multiple testing

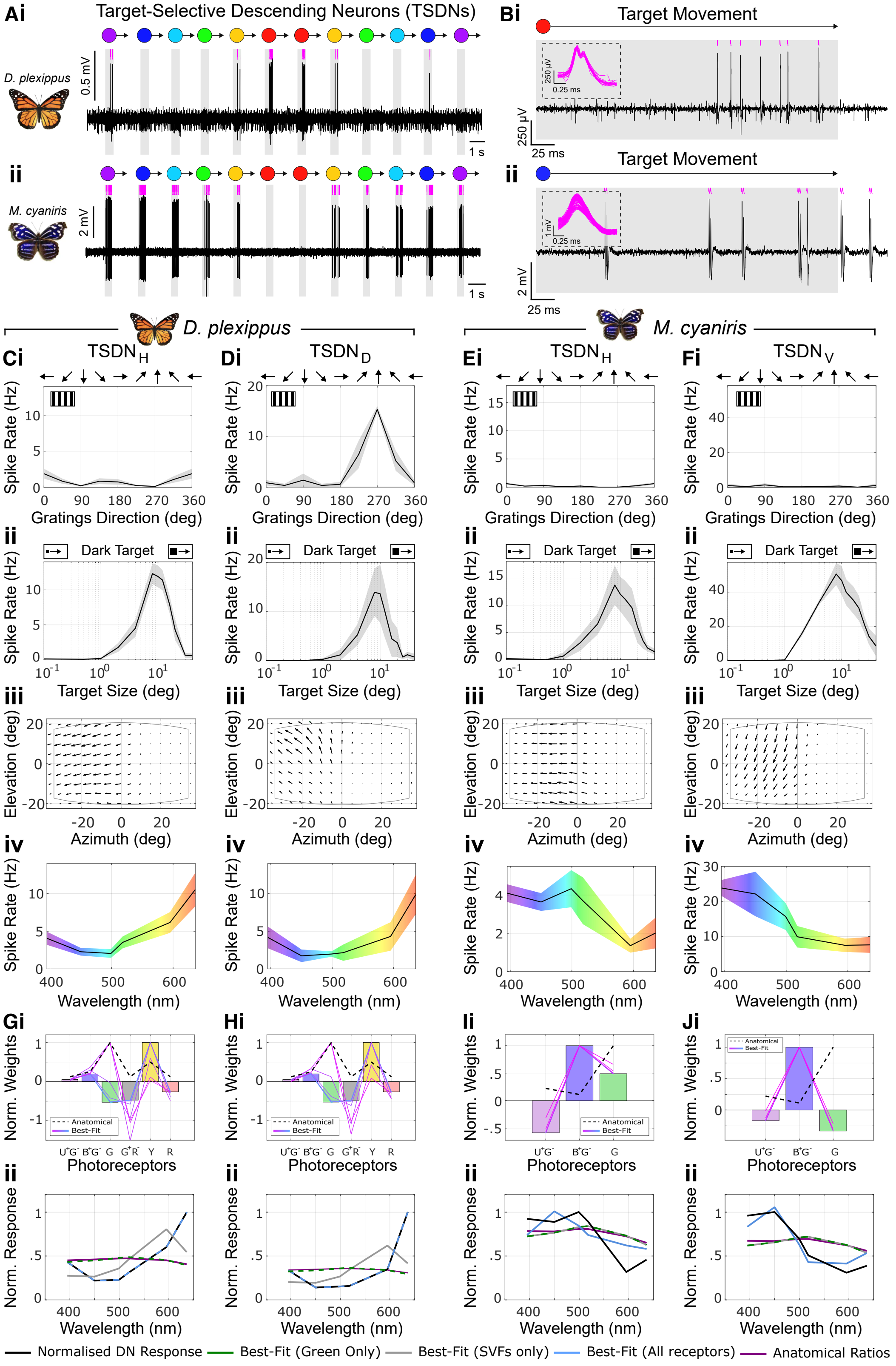

Figure 5. TSDN spectral sensitivities in *D. plexippus* and *M. cyaniris*

(A) Example raw extracellular voltage traces of TSDNs in (i) *D. plexippus* and (ii) male *M. cyaniris* responding to 8°-diameter circular bright targets of different color moving in the preferred direction. Gray regions indicate periods of target movement. Magenta lines show the sorted spikes from each TSDN unit.

(legend continued on next page)

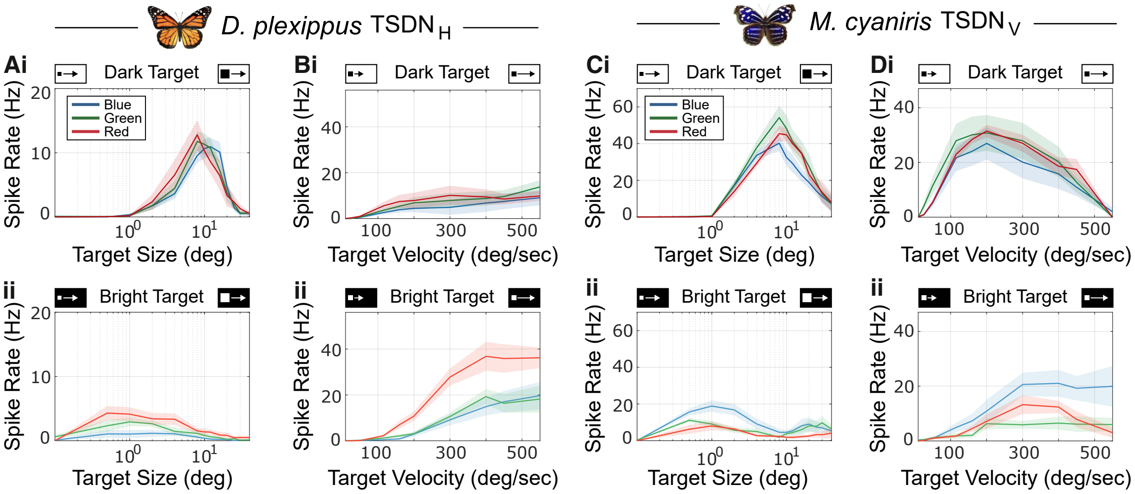

Figure 6. TSDN size and velocity tuning

Extended stimuli for (A and B) *D. plexippus* TSDN$_\text{H}$ (N = 10 units from 8 animals) and (C and D) *M. cyaniris* TSDN$_\text{V}$ (N = 6 units from 6 animals). Blue/green/red lines for blue/green/red DLP stimuli. (A and C) Size tuning curves for (i) dark and (ii) bright square objects moving in the preferred direction at constant 115°/s velocity. (B and D) Velocity tuning curves for (i) dark and (ii) bright square objects with constant side lengths subtending 4° and moving in the preferred direction. See Figure S3 for statistical analysis. *D. plexippus* TSDN$_\text{H}$ (N = 10 cells from 8 animals). *M. cyaniris* TSDN$_\text{V}$ (N = 6 cells from 6 animals). Data show mean ± SEM. See also Figures S1 and S5.

($p > 0.05$, N = 20 animals. Figures S4C–S4H). We therefore proceeded to investigate putative functional relationships between TSDN spectral sensitivity and goal-directed behavior by comparing the alignment of TSDN spectral sensitivities with conspecific wing reflectance (Figure 7).

We calculated spectral alignment as the cosine similarity between spectral functions (equivalent to the Pearson correlation coefficient, PCC, for two vectors; Figures 7Ciii and 7Fiii). In *Danaus*, TSDN spectral tuning was closely aligned to wing reflectance (TSDN$_\text{H}$: PCC = 0.95; TSDN$_\text{D}$: PCC = 0.82; Figures 7Ciii and 7Diii). The near-perfect matching between *Danaus* TSDN$_\text{H}$ and wing reflectance was primarily impeded by the increase in TSDN UV-blue sensitivity of between 395 and 450 nm. In *Myscelia*, wing reflectance spectra were less closely aligned to TSDN spectral sensitivities (TSDN$_\text{H}$: PCC = 0.60; TSDN$_\text{V}$: PCC = 0.85; Figures 7Eiii and 7Fiii), attributable to the rightward shift in TSDN spectral maxima (TSDN$_\text{H}$ maximum: 470 nm; TSDN$_\text{V}$ maximum: 420 nm) from the maximum wing reflectance (maximum: 370 nm).

However, our measurements of wing reflectance spectra were acquired using calibrated white light, producing the standardized reflectance (Figure 7A). In nature, the reflected photon radiance depends on both the wing reflectance and the spectral content of the natural illuminant (usually skylight; Figure 7A),[132] which is attenuated below 450 nm (Figure 7B).[133,134] To simulate reflected photon radiance under natural conditions, we multiplied the wing reflectance with the standard daylight illuminant, CIED65 (Figure 7B). The reflected photon radiance of *Danaus* wings closely resembles reflectance due to the relatively flat skylight spectrum above 450 nm (Figure 7B), with a slight reduction in spectral alignment of ∼2% to PCC = 0.94 in TSDN$_\text{H}$ and ∼3% to PCC = 0.81 in TSDN$_\text{D}$ (Figures 7Ciii and 7Diii). However, due to skylight short-wavelength attenuation, the natural reflected photon radiance maximum of male *Myscelia* wings shifted from 370s to 410 nm (Figure 7B). This rightward shift increases alignment with *Myscelia* TSDN spectral tuning, increasing by ∼15% to PCC = 0.72 in TSDN$_\text{H}$ and ∼9% to PCC = 0.93 in TSDN$_\text{V}$ (Figures 7Eiii and 7Fiii).

DISCUSSION

Overall, we observed a separation of spectral sensitivities in butterfly DNs, which aligned with functional differences in motion

(B) Expanded time view of the maximum target responses in (A). Inset shows spike-sorted waveforms for the unit in (A). Note that the example *Danaus* waveform coincides with spikes from another DN, resulting in the dip in peak voltage.

(C–F) TSDN responses from (C and D) *D. plexippus* (TSDN$_\text{H}$, N = 11 units from 9 animals; TSDN$_\text{D}$, N = 3 units from 2 animals) and (E and F) *M. cyaniris* (TSDN$_\text{H}$, N = 5 units from 4 males; TSDN$_\text{V}$, N = 6 units from 5 males). (i–iv) Stimuli same as in Figures 2D and 2E. (i) Moving gratings; (ii) dark objects of different sizes; (iii) receptive fields; (iv) spectral tuning curves. See Figures 2D and 2E legend for details. TSDN$_\text{H}$/TSDN$_\text{D}$/TSDN$_\text{V}$ refer to horizontal, dorsal, and ventral preferred direction of motion, respectively, as determined from the receptive fields in (iii). Data show mean ± SEM.

(G–J) Modeled TSDN LED-galvo responses from linear combinations of photoreceptor inputs for (G and H) *D. plexippus* and (I and J) *M. cyaniris*. Same model as used in Figures 2F and 2G. (i) Least-squares best-fit photoreceptor weights that reproduce TSDN spectral sensitivity. Bars correspond to the overall best-fit photoreceptor weights. Blue-magenta best-fit lines show all possible photoreceptor weight combinations that reproduce DN responses with $R^2 \geq 90\%$ the overall best-fit value. Dashed black line shows anatomical photoreceptor ratios. (ii) Least-squares best-fit TSDN responses for (dashed green) green-only input, (gray) SVF-only inputs, (dashed blue) all photoreceptors, and (purple) anatomically informed photoreceptor ratio estimates. Black line shows normalized WFDN$_\text{H}$ response measured with the LED-galvo. Note that black and dashed blue curves overlay precisely for *Danaus*.

See also Figures S1 and S5.

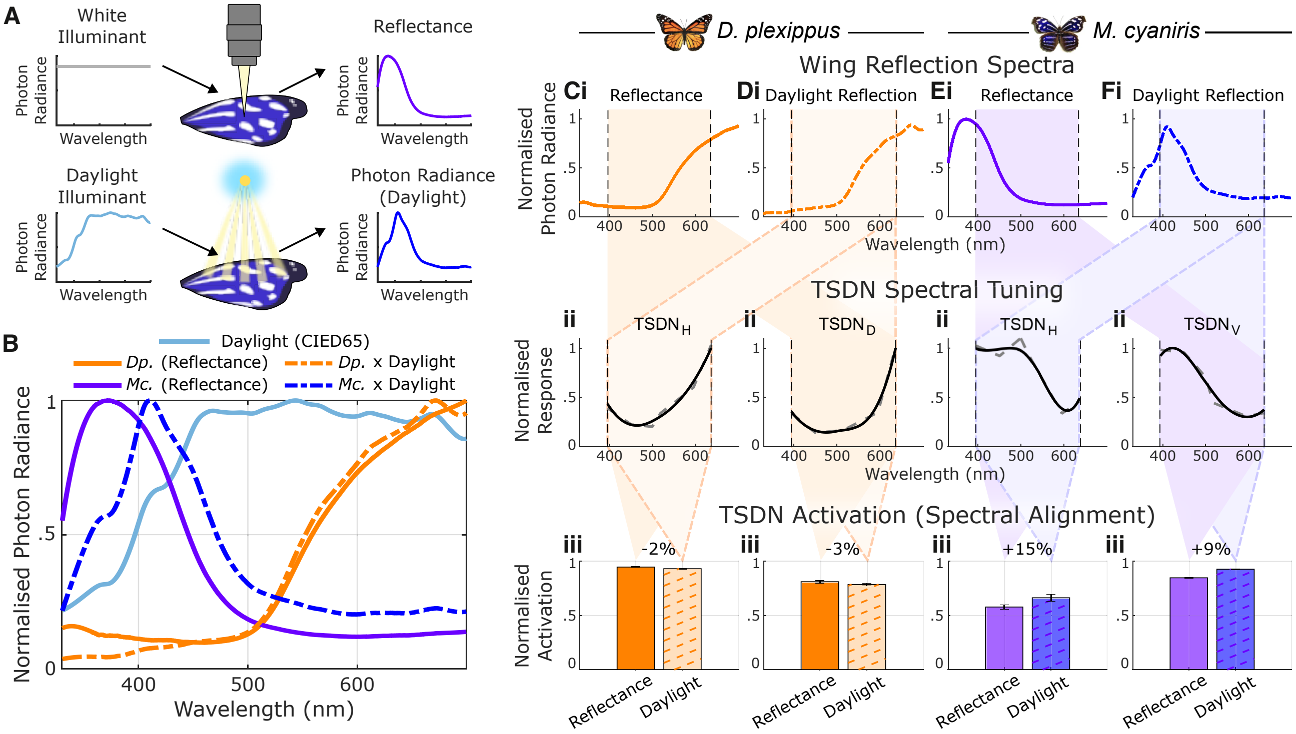

Figure 7. Butterfly TSDN spectral tuning matches conspecific wing reflections under daylight illuminant

(A) Wing reflectance is a standardized metric referring to the fraction of illuminant photon radiance reflected as a function of wavelength. The normalized (i.e., unitless) wing reflectance spectrum therefore equals the normalized reflected photon radiance under a calibrated white illuminant. Under natural conditions, however, the spectral content of reflected photon radiance is a combination of both the wing reflectance and the illuminant (e.g., daylight).

(B) Comparison of normalized wing reflectance (solid lines) and estimates of natural wing reflection under daylight (dashed lines), calculated by multiplying wing reflectance with the standard average daylight illuminant, CIED65. *Dp*, *D. plexippus*; *Mc*, *M. cyaniris*.

(C–F) Spectral alignment between (i) wing reflectance and reflected daylight photon radiance and (ii) TSDN spectral tuning. Raw average TSDN tuning curve (dashed gray) shown with smoothed TSDN tuning curve (black). (iii) Spectral alignment is calculated as the cosine similarity across the 395–636 nm range (i.e., the range used for TSDN measurements). Percentage changes in spectral alignment between standard wing reflectance (solid color) and daylight wing reflection (dashed) are displayed. Error bars represent standard deviation of alignment estimates for different levels of TSDN tuning curve smoothing (see Figures S5J–S5L). See also Video S3.

sensitivity. Butterfly WFDN activity closely resembles those described in other species,[43–55] with a maximum sensitivity to wide-field motion along a preferred direction (Figure 2). Butterfly WFDNs have effective broadband spectral responses (Figures 2Div and 2Eiv), although subtle species-specific differences in WFDN spectral tuning corresponds with both the available set of photoreceptors (Figure 1C) and the spectral sensitivity of optomotor head rotations (Figure 4), supporting the involvement of WFDNs in controlling stabilization reflexes.[43] In contrast to WFDNs, butterfly TSDNs are comparatively narrowband (Figures 5Civ–5Fiv) and match conspecific wing coloration (Figure 7), suggesting a role in coordinating sexual pursuit behavior.

Indeed, butterfly TSDNs sample from the frontal visual field, aligning with optical acute zone specializations for target tracking described in other Nymphalids.[135,136] In sexually dimorphic butterflies, male wing coloration signals both sexual fitness to the female and sexual identity to repel unwanted male advances.[108,109] While little is reported regarding *Myscelia* behavior, males in captivity readily engage in fast aerial pursuits and perch with their dorsal wing coloration displayed (Video S3), similar to other species with prominent dorsal wing coloration.[109] The tuning of male *Myscelia* TSDNs to male wing coloration suggests a potential role in territorial pursuit, and future work should investigate whether female TSDNs have similar spectral selectivity. In *Danaus*, TSDNs in both sexes are exquisitely tuned to long wavelengths (Figures S5C–S5G). Notably, wing coloration in *Danaus* is sexually monomorphic due to the constraint of Müllerian mimicry, whereby divergence from the population visual trait is penalized by increased predation.[127,137] *Danaus* may therefore rely more on olfaction to determine mate suitability.[138,139] Indeed, males engage in aerial "hair-penciling" to disseminate pheromones over the female antennae during courtship flight.[100,104,106,140] In Noctuid moths, female pheromone produces upwind flight in males by amplifying WFDN sensitivity[52] and optomotor reflexes[141,142]; future work should investigate whether olfaction modulates butterfly TSDN responses in a similarly sexually dimorphic manner.

Response characteristics of butterfly TSDNs largely resemble those described in Diptera[40,50,65,66] and Odonata.[59–62,78] However, while most TSDNs responded exclusively to moving targets, *Danaus* TSDN$_D$ also responded to gratings moving in the preferred direction, albeit at a lower firing rate than typical of WFDNs. Butterfly TSDN size tuning is similar to that of Dipteran TSDNs,[40,50] but it is sensitive to larger targets than dragonfly TSDNs.[78] However, dragonfly TSDN target size preference ranges from 1° diameter in bright skylight to 16° in a dim laboratory due to light adaptation,[78] thus butterfly TSDNs may display similar variability as a function of adapting background luminance. Notably, preferred target sizes were smaller for bright targets compared with dark targets (Figures 6A and 6C). The irradiation illusion is a similar phenomenon in human vision, whereby a bright object on a dark background appears larger than the same-sized object with opposite contrast.[143,144] This arises from a saturating non-linearity in ON-contrast sensitivity compared with near-linear OFF-contrast sensitivity.[145,146] However, the magnification factor of the irradiation illusion in humans is ∼1.5×,[144] so other mechanisms may be involved in the ∼8× increase in preferred size observed in butterfly TSDNs.

While butterfly TSDN spectral, size, and velocity tuning suggests involvement in sexual pursuit behavior, flowers subtend similar visual angles as butterflies during flight, and it is likely that DN populations function collectively to support multiple behaviors to minimize energetic expenditure.[50,147] Many insects display innate spectral preferences for various behaviors including feeding, mating, and oviposition.[148–151] Interestingly, while spectral preferences often differ between behaviors,[110,152] some species, including *Danaus*, have an innate preference to feed from flowers spectrally similar to conspecific coloration.[153,154] Innate spectral preferences readily shift to other wavelengths upon training,[150,154] and they coincide with spectral re-tuning of mushroom body neurons.[122] Testing whether butterfly TSDNs display comparable spectral plasticity will provide insight into their involvement in controlling foraging behaviors.

Nonetheless, the difference in spectral sensitivities between butterfly WFDNs and TSDNs indicates a functional separation of spectral inputs to motion vision in the context of stabilization reflexes and target tracking, respectively. Diurnal insect optomotor systems usually receive input from SVF photoreceptors expressing green-peaking opsin with effective broadband sensitivity.[82–95] This broad spectral sensitivity increases photon catch that, in addition to the quadratic sensitivity to image contrast in elementary movement detection,[155] produces a stabilization system robust to variations in image statistics while the animal moves through the environment.[92] Additional photoreceptors converge onto wide-field motion vision in *Drosophila*[32] and bees,[79] further improving the sensitivity and spectral range of optomotor reflexes.[32] Electrophysiological and connectomic data demonstrate that multiple photoreceptor inputs broaden the spectral sensitivity of most LMCs in *Papilio* butterflies.[95,125] We found that *Myscelia* WFDN$_H$ and optomotor responses could be well explained by predominantly green and B^+G^- photoreceptor input (Figures 2Giii–2Giv). *Danaus* displayed a reduction in wide-field blue sensitivity and an increase in red sensitivity, which were not explained by green-only or SVF-only photoreceptor absorption (Figure 2Fiv), suggesting that a combination of SVFs and LVFs contribute to optomotor-related motion vision (Figure 2Fiii). Further analysis of WFDN$_H$ and optomotor response half-saturation stimulus intensities,[71,87,95,148,156,157] in combination with opsin photobleaching,[158,159] will be required to unambiguously determine the photoreceptor identities contributing to wide-field responses in *Danaus*. Nonetheless, broad spectral tuning of the optomotor system may be a general optimization for producing consistent stabilizing movements that are fast, sensitive, and robust to changes in the spectral content of the environment.[92]

However, what selective pressures drive the reduced blue sensitivity and increased red sensitivity of the wide-field system in *Danaus*? The inclusion of motion-vision red sensitivity could come at the cost of blue sensitivity, or alternatively, the exclusion of blue sensitivity could improve red sensitivity. Previous work in *Danaus* reported that (1) red-sensitive R9 inhibits G^+R^--opponent R1-2, photoreceptors that are usually UV or blue sensitive in simple retinas, and (2) blue-sensitive photoreceptors are long-wavelength inhibited.[121,131] While long-wavelength vision in *Danaus* matches conspecific wing coloration, red receptors may have other general advantages for motion vision. For example, foliage has broad reflectance extending toward long wavelengths, with average flower reflectance continuing to increase beyond 700 nm.[160] Further analysis of wide-field motion vision in butterflies with red-sensitive retinas will be required to determine the prevalence and functional advantages of motion-vision red sensitivity, especially in species with non-red wing coloration such as *Papilio*[161] or *Pieris*.[162,163]

A previous investigation of TSDN spectral sensitivities reported adaptations to improve photon catch,[71] reminiscent of optomotor spectral broadening.[32] Dragonflies hunt from below to contrast flying prey silhouettes against the sky,[74–76] and their TSDNs are correspondingly aligned to sample the dorsal visual field[60–62] with a maximum spectral sensitivity to UV/blue.[71] This matches the enrichment of UV/blue sensitivity in the dorsal retina,[72] along with other optical and physiological specializations that enhance skylight photon catch.[77] The narrowband spectral tuning of butterfly TSDNs suggests that despite lower total photon catch, target-tracking signal to noise is overall enhanced by band-pass spectral filtering matched to the coloration of interest. However, whether TSDN spectral selectivity arises directly at the level of motion detection in the optic lobe or via convergence of chromatic input onto an otherwise achromatic motion-vision pathway remains to be tested. In *Sarcophaga* blowflies, male-specific TSDNs have secondary arborizations in the anterior optic tubercle,[65] a target neuropil for processing polarization and chromatic outputs from the optic lobe,[164,165] suggesting a potential convergence of parallel chromatic/achromatic inputs.

However, asymmetric spectral sensitivities of ON and OFF pathways in *Drosophila* motion-sensitive T4/T5 cells enhance the detection of approaching objects that differ in color to the background,[20] demonstrating advantages for intrinsically chromatic motion vision. Notably, *Myscelia* TSDN responses to dark objects on bright backgrounds were less sensitive when the background was blue (Figure 4Mi), opposite to the maximum sensitivity to bright blue objects moving on a dark background (Figure 4Mii). This could indicate differences in ON/OFF spectral sensitivities in the target-tracking pathway, analogous to that described in *Drosophila* T4/T5 cells.[20] Future work should determine the origin of spectral selectivity in butterfly TSDNs and model target-tracking performance for both direct and convergent configurations. This will provide potentially generalizable insights into the advantages of spectrally selective motion vision, with applications to artificial vision systems.

RESOURCE AVAILABILITY

Lead contact

Requests for further information and resources should be directed to and will be fulfilled by the lead contact, Jack A. Supple (jackalexsupple@gmail.com).

Materials availability

This study did not generate new, unique materials.

Data and code availability

All wing reflectance, photoreceptor spectral sensitivity, DN electrophysiology, and optomotor response data have been deposited at Zenodo.org and are publicly available as of the date of publication at Zenodo: https://doi.org/10.5281/zenodo.17604651. All original code has been deposited at GitHub and is publicly available at GitHub: https://github.com/jacksupple/Supple_2025_butterfly_spectral_tuning as of the date of publication. Any additional information required to reanalyze the data reported in this paper is available from the lead contact upon request.

ACKNOWLEDGMENTS

This work was supported by Air Force Office of Scientific Research (AFOSR) grant FA8655-23-1-7049 to G.B. and H.G.K., Biotechnology and Biological Sciences Research Council (BBSRC) grant BB/X002276/1 to H.G.K., and Bio-inspired Sensing Computing and Control with International Teams (BISCCITs) travel grant to J.A.S. Thanks to Ric Wehling and Nandini Iyer for providing financial support.

AUTHOR CONTRIBUTIONS

Conceptualization, J.A.S., G.B., and H.G.K.; methodology, J.A.S., U.C., M.I., A.S., P.P., and G.B.; software, J.A.S., U.C., M.I., A.S., and G.B.; formal analysis, J.A.S.; investigation, J.A.S., U.C., and G.B.; resources, J.A.S., A.S., G.B., and H.G.K.; writing – original draft, J.A.S.; writing – review & editing, J.A.S., U.C., M.I., A.S., P.P., G.B., and H.G.K.; visualization, J.A.S., U.C., and P.P.; supervision, G.B. and H.G.K.; project administration, J.A.S., G.B., and H.G.K.; funding acquisition, J.A.S., G.B., and H.G.K.

DECLARATION OF INTERESTS

The authors declare no competing interests.

DECLARATION OF GENERATIVE AI AND AI-ASSISTED TECHNOLOGIES IN THE WRITING PROCESS

During the preparation of this work the author(s) used ChatGPT-5 to generate code, check written grammar, and find source material. After using this tool/service, the author(s) reviewed and edited the content as needed and take full responsibility for the content of the published article.

STAR★METHODS

Detailed methods are provided in the online version of this paper and include the following:

- KEY RESOURCES TABLE
- EXPERIMENTAL MODEL AND STUDY PARTICIPANT DETAILS
    - ○ Animals
- METHOD DETAILS
    - ○ Wing reflectance measurements
    - ○ Visual stimuli
    - ○ Photoreceptor electrophysiology
    - ○ Descending neuron electrophysiology
    - ○ Modelling DN responses from photoreceptor inputs
    - ○ Head movements
- QUANTIFICATION AND STATISTICAL ANALYSIS
    - ○ Descending neuron electrophysiology
    - ○ Head movements
    - ○ Spectral alignment calculations

SUPPLEMENTAL INFORMATION

Supplemental information can be found online at https://doi.org/10.1016/j.cub.2025.11.037.

Received: August 10, 2025
Revised: October 7, 2025
Accepted: November 14, 2025
Published: December 22, 2025

REFERENCES

1. Dorkenwald, S., Matsliah, A., Sterling, A.R., Schlegel, P., Yu, S.C., McKellar, C.E., Lin, A., Costa, M., Eichler, K., Yin, Y., et al. (2024). Neuronal wiring diagram of an adult brain. Nature *634*, 124–138. https://doi.org/10.1038/s41586-024-07558-y.
2. Godfrey, R.K., Swartzlander, M., and Gronenberg, W. (2021). Allometric analysis of brain cell number in Hymenoptera suggests ant brains diverge from general trends. Proc. Biol. Sci. *288*, 20210199. https://doi.org/10.1098/rspb.2021.0199.
3. Raji, J.I., and Potter, C.J. (2021). The number of neurons in Drosophila and mosquito brains. PLOS One *16*, e0250381. https://doi.org/10.1371/journal.pone.0250381.
4. Woods, W.A., Jr., Heinrich, B., and Stevenson, R.D. (2005). Honeybee flight metabolic rate: does it depend upon air temperature? J. Exp. Biol. *208*, 1161–1173. https://doi.org/10.1242/jeb.01510.
5. Niven, J.E., and Scharlemann, J.P.W. (2005). Do insect metabolic rates at rest and during flight scale with body mass? Biol. Lett. *1*, 346–349. https://doi.org/10.1098/rsbl.2005.0311.
6. Hernández, D.G., Rivera, C., Cande, J., Zhou, B., Stern, D.L., and Berman, G.J. (2021). A framework for studying behavioral evolution by reconstructing ancestral repertoires. eLife *10*, e61806. https://doi.org/10.7554/eLife.61806.
7. Gilbert, C. (1997). Visual control of cursorial prey pursuit by tiger beetles (Cicindelidae). J. Comp. Physiol., A *181*, 217–230. https://doi.org/10.1007/s003590050108.
8. Land, M.F., and Collett, T.S. (1974). Chasing behaviour of houseflies (Fannia canicularis) – A description and analysis. J. Comp. Physiol. *89*, 331–357. https://doi.org/10.1007/BF00695351.
9. de Croon, G.C.H.E., Dupeyroux, J.J.G., Fuller, S.B., and Marshall, J.A.R. (2022). Insect-inspired AI for autonomous robots. Sci. Robot. *7*, eabl6334. https://doi.org/10.1126/scirobotics.abl6334.
10. Wehner, R. (1987). "Matched filters" – neural models of the external world. J. Comp. Physiol. *161*, 511–531. https://doi.org/10.1007/BF00603659.
11. Warrant, E.J. (2016). Matched Filtering and the Ecology of Vision in Insects. In The Ecology of Animal Senses, G. Von Der Emde, and E. Warrant, eds. (Springer International Publishing), pp. 143–167. https://doi.org/10.1007/978-3-319-25492-0_6.
12. Krapp, H.G. (2000). Neuronal Matched Filters for Optic Flow Processing in Flying Insects. In Int. Rev. Neurobiol., *44* (Elsevier), pp. 93–120. https://doi.org/10.1016/S0074-7742(08)60739-4.
13. Sterling, P., and Laughlin, S. (2015). Principles of Neural Design (The MIT Press). https://doi.org/10.7551/mitpress/9780262028707.001.0001.
14. Krapp, H.G., and Wicklein, M. (2008). Central Processing of Visual Information in Insects. In The Senses: A Comprehensive Reference (Elsevier Incorporated), pp. 131–203. https://doi.org/10.1016/B978-012370880-9.00262-0.

15. Krapp, H.G., Taylor, G.K., and Humbert, J.S. (2012). The mode-sensing hypothesis: Matching sensors, actuators and flight dynamics. In Frontiers in Sensing (Springer Vienna), pp. 101–114. https://doi.org/10.1007/978-3-211-99749-9_7.
16. Humbert, J.S., Krapp, H.G., Baeder, J.D., Badrya, C., Dawson, I.L., Huang, J.V., Hyslop, A., Jung, Y.S., Leroy, A., Lutkus, C., et al. (2024). Motion vision is tuned to maximize sensorimotor energy transfer in blowfly flight. Preprint at bioRxiv. https://doi.org/10.1101/2024.03.29.587347.
17. Turin, Z., Taylor, G.K., Krapp, H.G., Jensen, E., and Sean Humbert, J. (2025). Matching Sensing to Actuation and Dynamics in Distributed Sensorimotor Architectures. IEEE Access *13*, 13584–13605. https://doi.org/10.1109/ACCESS.2025.3528343.
18. Wernet, M.F., Perry, M.W., and Desplan, C. (2015). The evolutionary diversity of insect retinal mosaics: Common design principles and emerging molecular logic. Trends Genet. *31*, 316–328. https://doi.org/10.1016/j.tig.2015.04.006.
19. Kelber, A., and Osorio, D. (2010). From spectral information to animal colour vision: experiments and concepts. Proc. Biol. Sci. *277*, 1617–1625. https://doi.org/10.1098/rspb.2009.2118.
20. Longden, K.D., Rogers, E.M., Nern, A., Dionne, H., and Reiser, M.B. (2023). Different spectral sensitivities of ON- and OFF-motion pathways enhance the detection of approaching color objects in Drosophila. Nat. Commun. *14*, 7693. https://doi.org/10.1038/s41467-023-43566-8.
21. Conway, B.R. (2014). Color signals through dorsal and ventral visual pathways. Vis. Neurosci. *31*, 197–209. https://doi.org/10.1017/S0952523813000382.
22. Paulk, A.C., Phillips-Portillo, J., Dacks, A.M., Fellous, J.-M., and Gronenberg, W. (2008). The Processing of Color, Motion, and Stimulus Timing Are Anatomically Segregated in the Bumblebee Brain. J. Neurosci. *28*, 6319–6332. https://doi.org/10.1523/JNEUROSCI.1196-08.2008.
23. Rivera-Alba, M., Vitaladevuni, S.N., Mishchenko, Y., Lu, Z., Takemura, S.Y., Scheffer, L., Meinertzhagen, I.A., Chklovskii, D.B., and de Polavieja, G.G. (2011). Wiring Economy and Volume Exclusion Determine Neuronal Placement in the *Drosophila* Brain. Curr. Biol. *21*, 2000–2005. https://doi.org/10.1016/j.cub.2011.10.022.
24. Strausfeld, N.J. (1971). The organization of the insect visual system (Light microscopy): I. Projections and Arrangements of Neurons in the Lamina ganglionaris of Diptera. Z. Zellforsch. *121*, 377–441. https://doi.org/10.1007/BF00337640.
25. Fischbach, K.F., and Dittrich, A.P.M. (1989). The optic lobe of Drosophila melanogaster. I. A Golgi analysis of wild-type structure. Cell Tissue Res. *258*, 441–475. https://doi.org/10.1007/BF00218858.
26. Laughlin, S.B. (2017). Fly Optic Lamina as a Guide to Neural Circuit Design. In Handbook of Brain Microcircuits, G.M. Shepherd, and S. Grillner, eds. (Oxford University Press), pp. 285–292. https://doi.org/10.1093/med/9780190636111.003.0023.
27. Strausfeld, N.J., and Lee, J.K. (1991). Neuronal basis for parallel visual processing in the fly. Vis. Neurosci. *7*, 13–33. https://doi.org/10.1017/S0952523800010919.
28. Paulk, A.C., Dacks, A.M., Phillips-Portillo, J., Fellous, J.-M., and Gronenberg, W. (2009). Visual Processing in the Central Bee Brain. J. Neurosci. *29*, 9987–9999. https://doi.org/10.1523/JNEUROSCI.1325-09.2009.
29. Longden, K.D. (2016). Central Brain Circuitry for Color-Vision-Modulated Behaviors. Curr. Biol. *26*, R981–R988. https://doi.org/10.1016/j.cub.2016.07.071.
30. van Hateren, J.H., Rüttiger, L., Sun, H., and Lee, B.B. (2002). Processing of Natural Temporal Stimuli by Macaque Retinal Ganglion Cells. J. Neurosci. *22*, 9945–9960. https://doi.org/10.1523/JNEUROSCI.22-22-09945.2002.
31. Giurfa, M., and Vorobyev, M. (1998). The angular range of achromatic target detection by honey bees. J. Comp. Physiol., A *183*, 101–110. https://doi.org/10.1007/s003590050238.
32. Wardill, T.J., List, O., Li, X., Dongre, S., McCulloch, M., Ting, C.Y., O'Kane, C.J., Tang, S., Lee, C.H., Hardie, R.C., et al. (2012). Multiple spectral inputs improve motion discrimination in the drosophila visual system. Science *336*, 925–931. https://doi.org/10.1126/science.1215317.
33. Schnaitmann, C., Garbers, C., Wachtler, T., and Tanimoto, H. (2013). Color Discrimination with Broadband Photoreceptors. Curr. Biol. *23*, 2375–2382. https://doi.org/10.1016/j.cub.2013.10.037.
34. Céchetto, C., Arikawa, K., and Kinoshita, M. (2022). Motion-sensitive neurons activated by chromatic contrast in a butterfly visual system. Philos. Trans. R. Soc. Lond. B Biol. Sci. *377*, 20210277. https://doi.org/10.1098/rstb.2021.0277.
35. Stewart, F.J., Kinoshita, M., and Arikawa, K. (2015). The butterfly Papilio xuthus detects visual motion using chromatic contrast. Biol. Lett. *11*, 20150687. https://doi.org/10.1098/rsbl.2015.0687.
36. Maisak, M.S., Haag, J., Ammer, G., Serbe, E., Meier, M., Leonhardt, A., Schilling, T., Bahl, A., Rubin, G.M., Nern, A., et al. (2013). A directional tuning map of Drosophila elementary motion detectors. Nature *500*, 212–216. https://doi.org/10.1038/nature12320.
37. Namiki, S., Dickinson, M.H., Wong, A.M., Korff, W., and Card, G.M. (2018). The functional organization of descending sensory-motor pathways in Drosophila. eLife *7*, e34272. https://doi.org/10.7554/eLife.34272.
38. Simpson, J.H. (2024). Descending control of motor sequences in Drosophila. Curr. Opin. Neurobiol. *84*, 102822. https://doi.org/10.1016/j.conb.2023.102822.
39. Parsons, M.M., Krapp, H.G., and Laughlin, S.B. (2010). Sensor Fusion in Identified Visual Interneurons. Curr. Biol. *20*, 624–628. https://doi.org/10.1016/j.cub.2010.01.064.
40. Nicholas, S., Supple, J., Leibbrandt, R., Gonzalez-Bellido, P.T., and Nordström, K. (2018). Integration of Small- and Wide-Field Visual Features in Target-Selective Descending Neurons of both Predatory and Nonpredatory Dipterans. J. Neurosci. *38*, 10725–10733. https://doi.org/10.1523/JNEUROSCI.1695-18.2018.
41. Olberg, R.M. (1981). Object- and self-movement detectors in the ventral nerve cord of the dragonfly. J. Comp. Physiol. *141*, 327–334. https://doi.org/10.1007/BF00609935.
42. Collett, T.S. (1980). Angular tracking and the optomotor response an analysis of visual reflex interaction in a hoverfly. J. Comp. Physiol. *140*, 145–158. https://doi.org/10.1007/BF00606306.
43. Wertz, A., Gaub, B., Plett, J., Haag, J., and Borst, A. (2009). Robust Coding of Ego-Motion in Descending Neurons of the Fly. J. Neurosci. *29*, 14993–15000. https://doi.org/10.1523/JNEUROSCI.3786-09.2009.
44. Haag, J., Wertz, A., and Borst, A. (2007). Integration of Lobula Plate Output Signals by DNOVS1, an Identified Premotor Descending Neuron. J. Neurosci. *27*, 1992–2000. https://doi.org/10.1523/JNEUROSCI.4393-06.2007.
45. Goodman, L.J., Fletcher, W.A., Guy, R.G., Mobbs, P.G., and Pomfrett, C.D.J. (1987). Motion Sensitive Descending Interneurons, Ocellar LD Neurons and Neck Motoneurons in the Bee: A Neural Substrate for Visual Course Control in Apis mellifera. In Neurobiology and Behavior of Honeybees, R. Menzel, and A. Mercer, eds. (Springer Berlin Heidelberg), pp. 158–171. https://doi.org/10.1007/978-3-642-71496-2_14.
46. Gronenberg, W., Milde, J.J., and Strausfeld, N.J. (1995). Oculomotor control in calliphorid flies: Organization of descending neurons to neck motor neurons responding to visual stimuli. J. Comp. Neurol. *361*, 267–284. https://doi.org/10.1002/cne.903610206.
47. Gronenberg, W., and Strausfeld, N.J. (1990). Descending neurons supplying the neck and flight motor of Diptera: Physiological and anatomical characteristics. J. Comp. Neurol. *302*, 973–991. https://doi.org/10.1002/cne.903020420.

48. Ibbotson, M.R. (1991). A motion-sensitive visual descending neurone in Apis mellifera monitoring translatory optic flow-fields in the horizontal plane. J. Exp. Biol. *157*, 573–577. https://doi.org/10.1242/jeb.157.1.573.

49. Ibbotson, M.R., and Goodman, L.J. (1990). Response characteristics of four wide-field motion- sensitive descending interneurones in Apis mellifera. J. Exp. Biol. *148*, 255–279. https://doi.org/10.1242/jeb.148.1.255.

50. Nicholas, S., Leibbrandt, R., and Nordström, K. (2020). Visual motion sensitivity in descending neurons in the hoverfly. J. Comp. Physiol. A Neuroethol. Sens. Neural Behav. Physiol. *206*, 149–163. https://doi.org/10.1007/s00359-020-01402-0.

51. Olberg, R.M. (1981). Parallel Encoding of Direction of Wind, Head, Abdomen, and Visual Pattern Movement by Single Interneurons in the Dragonfly. J. Comp. Physiol. *142*, 27–41. https://doi.org/10.1007/BF00605473.

52. Olberg, R.M., and Willis, M.A. (1990). Pheromone-modulated optomotor response in male gypsy moths, Lymantria dispar L.: Directionally selective visual interneurons in the ventral nerve cord. J. Comp. Physiol. A *167*, 707–714. https://doi.org/10.1007/BF00192665.

53. Singarajah, K.V. (1988). Spectral sensitivity of motion-sensitive units of the butterfly ventral nerve cord. J. Insect Physiol. *34*, 1005–1012. https://doi.org/10.1016/0022-1910(88)90199-0.

54. Suver, M.P., Huda, A., Iwasaki, N., Safarik, S., and Dickinson, M.H. (2016). An array of descending visual interneurons encoding self-motion in Drosophila. J. Neurosci. *36*, 11768–11780. https://doi.org/10.1523/JNEUROSCI.2277-16.2016.

55. Rowell, C.H.F., and Reichert, H. (1986). Three descending interneurons reporting deviation from course in the locust – II. Physiology. J. Comp. Physiol. A *158*, 775–794. https://doi.org/10.1007/BF01324821.

56. Wertz, A., Borst, A., and Haag, J. (2008). Nonlinear Integration of Binocular Optic Flow by DNOVS2, A Descending Neuron of the Fly. J. Neurosci. *28*, 3131–3140. https://doi.org/10.1523/JNEUROSCI.5460-07.2008.

57. Palmer, E.H., Omoto, J.J., and Dickinson, M.H. (2022). The role of a population of descending neurons in the optomotor response in flying Drosophila. Preprint at bioRxiv. https://doi.org/10.1101/2022.12.05.519224.

58. Sun, Q.-J. (1993). Response properties of descending object motion-detecting neurones in the ventral nerve cord of the common brown butterfly, *Heteronympha merope*. J. Insect Physiol. *39*, 1095–1100. https://doi.org/10.1016/0022-1910(93)90133-C.

59. Frye, M.A., and Olberg, R.M. (1995). Visual receptive field properties of feature detecting neurons in the dragonfly. J. Comp. Physiol. A *177*, 569–576. https://doi.org/10.1007/BF00207186.

60. Gonzalez-Bellido, P.T., Peng, H., Yang, J., Georgopoulos, A.P., and Olberg, R.M. (2013). Eight pairs of descending visual neurons in the dragonfly give wing motor centers accurate population vector of prey direction. Proc. Natl. Acad. Sci. USA *110*, 696–701. https://doi.org/10.1073/pnas.1210489109.

61. Olberg, R.M. (1986). Identified target-selective visual interneurons descending from the dragonfly brain. J. Comp. Physiol. *159*, 827–840. https://doi.org/10.1007/BF00603736.

62. Supple, J.A., Pinto-Benito, D., Khoo, C., Wardill, T.J., Fabian, S.T., Liu, M., Pusdekar, S., Galeano, D., Pan, J., Jiang, S., et al. (2020). Binocular Encoding in the Damselfly Pre-motor Target Tracking System. Curr. Biol. *30*, 645–656.e4. https://doi.org/10.1016/j.cub.2019.12.031.

63. Lin, H.-T., Siwanowicz, I., and Leonardo, A. (2024). Wireless recordings from dragonfly target detecting neurons during prey interception flight. Preprint at bioRxiv. https://doi.org/10.1101/2024.11.12.622977.

64. Perry, M.W., and Desplan, C. (2016). Love spots. Curr. Biol. *26*, R484–R485. https://doi.org/10.1016/j.cub.2016.02.020.

65. Gronenberg, W., and Strausfeld, N.J. (1991). Descending pathways connecting the male-specific visual system of flies to the neck and flight motor. J. Comp. Physiol. A *169*, 413–426. https://doi.org/10.1007/BF00197654.

66. Ogawa, Y., Nicholas, S., Thyselius, M., Leibbrandt, R., Nowotny, T., Knight, J.C., and Nordström, K. (2023). Descending neurons of the hoverfly respond to pursuits of artificial targets. Curr. Biol. *33*, 4392–4404.e5. https://doi.org/10.1016/j.cub.2023.08.091.

67. Barnett, P.D., Nordström, K., and O'Carroll, D.C. (2007). Retinotopic Organization of Small-Field-Target-Detecting Neurons in the Insect Visual System. Curr. Biol. *17*, 569–578. https://doi.org/10.1016/J.CUB.2007.02.039.

68. Nordström, K., Barnett, P.D., and O'Carroll, D.C. (2006). Insect detection of small targets moving in visual clutter. PLOS Biol. *4*, e54. https://doi.org/10.1371/journal.pbio.0040054.

69. Gilbert, C., and Strausfeld, N.J. (1991). The functional organization of male-specific visual neurons in flies. J. Comp. Physiol. A *169*, 395–411. https://doi.org/10.1007/BF00197653.

70. Strausfeld, N.J. (1991). Structural organization of male-specific visual neurons in calliphorid optic lobes. J. Comp. Physiol. A *169*, 379–393. https://doi.org/10.1007/BF00197652.

71. Horridge, G.A., Wang, X., and Zhang, S.W. (1990). Colour inputs to motion and object vision in an insect. Phil. Trans. R. Soc. Lond. B *329*, 257–263. https://doi.org/10.1098/rstb.1990.0169.

72. Labhart, T., and Nilsson, D.E. (1995). The dorsal eye of the dragonfly Sympetrum: specializations for prey detection against the blue sky. J. Comp. Physiol. A *176*, 437–453. https://doi.org/10.1007/BF00196410.

73. Laughlin, S.B. (1976). The sensitivities of dragonfly photoreceptors and the voltage gain of transduction. J. Comp. Physiol. *111*, 221–247. https://doi.org/10.1007/BF00606466.

74. Lin, H.T., and Leonardo, A. (2017). Heuristic Rules Underlying Dragonfly Prey Selection and Interception. Curr. Biol. *27*, 1124–1137. https://doi.org/10.1016/j.cub.2017.03.010.

75. Mischiati, M., Lin, H.-T., Herold, P., Imler, E., Olberg, R., and Leonardo, A. (2015). Internal models direct dragonfly interception steering. Nature *517*, 333–338. https://doi.org/10.1038/nature14045.

76. Olberg, R.M., Worthington, A.H., and Venator, K.R. (2000). Prey pursuit and interception in dragonflies. J. Comp. Physiol. A *186*, 155–162. https://doi.org/10.1007/s003590050015.

77. Laughlin, S., and McGinness, S. (1978). The structures of dorsal and ventral regions of a dragonfly retina. Cell Tissue Res. *188*, 427–447. https://doi.org/10.1007/BF00219782.

78. Olberg, R., and Pinter, R. (1990). The effect of mean luminance on the size selectivity of identified target interneurons in the dragonfly. J. Comp. Physiol. A *166*, 851–856. https://doi.org/10.1007/BF00187332.

79. Hung, Y.S., van Kleef, J.P., Stange, G., and Ibbotson, M.R. (2013). Spectral inputs and ocellar contributions to a pitch-sensitive descending neuron in the honeybee. J. Neurophysiol. *109*, 1202–1213. https://doi.org/10.1152/jn.00830.2012.

80. Bishop, L.G. (1969). A search for color encoding in the responses of a class of fly interneurons. Z. vergl. Physiologie *64*, 355–371. https://doi.org/10.1007/BF00340432.

81. Bishop, L.G. (1970). The spectral sensitivity of motion detector units recorded in the optic lobe of the honeybee. Z. Vergl. Physiol. *70*, 374–381. https://doi.org/10.1007/BF00298192.

82. McCann, G.D., and Arnett, D.W. (1972). Spectral and Polarization Sensitivity of the Dipteran Visual System. J. Gen. Physiol. *59*, 534–558. https://doi.org/10.1085/jgp.59.5.534.

83. Srinivasan, M.V., and Guy, R.G. (1990). Spectral properties of movement perception in the dronefly Eristalis. J. Comp. Physiol. A *166*, 287–295. https://doi.org/10.1007/BF00204803.

84. Heisenberg, M., and Buchner, E. (1977). The role of retinula cell types in visual behavior of Drosophila melanogaster. J. Comp. Physiol. *117*, 127–162. https://doi.org/10.1007/BF00612784.

85. Kaiser, W. (1974). The spectral sensitivity of the honeybee's optomotor walking response. J. Comp. Physiol. *90*, 405–408. https://doi.org/10.1007/BF00694179.

86. Kaiser, W. (1968). Zur Frage des Unterscheidungsvermögens für Spektralfarben: Eine Untersuchung der Optomotorik der königlichen Glanzfliege Phormia regina Meig. Z. vergl. Physiologie *61*, 71–102. https://doi.org/10.1007/BF00339146.

87. Kaiser, W., and Liske, E. (1974). Die optomotorischen Reaktionen von fixiert fliegenden Bienen bei Reizung mit Spektrallichtern. J. Comp. Physiol. *89*, 391–408. https://doi.org/10.1007/BF00695355.

88. Lehrer, M., Srinivasan, M.V., Zhang, S.W., and Horridge, G.A. (1997). Visual edge detection in the honeybee and its chromatic properties. Proc. R. Soc. Lond. B *238*, 321–330. https://doi.org/10.1098/rspb.1990.0002.

89. Lehrer, M., Wehner, R., and Srinivasan, M. (1985). Visual scanning behaviour in honeybees. J. Comp. Physiol. A *157*, 405–415. https://doi.org/10.1007/BF00615140.

90. Osorio, D. (1986). Ultraviolet Sensitivity and Spectral Opponency in the Locust. J. Exp. Biol. *122*, 193–208. https://doi.org/10.1242/jeb.122.1.193.

91. Schneider, G. (1956). Zur spektralen Empfindlichkeit des Komplexauges von Calliphora. Z. Vgl. Physiol. *39*, 1–20. https://doi.org/10.1007/BF00339170.

92. Srinivasan, M.V. (1985). Shouldn't directional movement detection necessarily be "colour-blind"? Vis. Res. *25*, 997–1000. https://doi.org/10.1016/0042-6989(85)90210-X.

93. Tinbergen, J., and Abeln, R.G. (1983). Spectral sensitivity of the landing blowfly. J. Comp. Physiol. *150*, 319–328. https://doi.org/10.1007/BF00605021.

94. Yamaguchi, S., Wolf, R., Desplan, C., and Heisenberg, M. (2008). Motion vision is independent of color in *Drosophila*. Proc. Natl. Acad. Sci. USA *105*, 4910–4915. https://doi.org/10.1073/pnas.0711484105.

95. Horridge, G.A., Marcelja, L., and Jahnke, R. (1984). Colour vision in butterflies: I. Single colour experiments. J. Comp. Physiol. *155*, 529–542. https://doi.org/10.1007/BF00611917.

96. Kawahara, A.Y., Storer, C., Carvalho, A.P.S., Plotkin, D.M., Condamine, F.L., Braga, M.P., Ellis, E.A., St Laurent, R.A., Li, X., Barve, V., et al. (2023). A global phylogeny of butterflies reveals their evolutionary history, ancestral hosts and biogeographic origins. Nat. Ecol. Evol. *7*, 903–913. https://doi.org/10.1038/s41559-023-02041-9.

97. Le Roy, C., Debat, V., and Llaurens, V. (2019). Adaptive evolution of butterfly wing shape: from morphology to behaviour. Biol. Rev. Camb. Philos. Soc. *94*, 1261–1281. https://doi.org/10.1111/BRV.12500.

98. Arikawa, K. (2017). The eyes and vision of butterflies. J. Physiol. *595*, 5457–5464. https://doi.org/10.1113/JP273917.

99. Baker, R.R. (1972). Territorial Behaviour of the Nymphalid Butterflies, Aglais urticae (L.) and Inachis io (L.). J. Anim. Ecol. *41*, 453–469. https://doi.org/10.2307/3480.

100. Brower, L.P., Brower, J.V.Z., and Cranston, F.P. (1965). Courtship behavior of the queen butterfly, Danaus gilippus berenice (Cramer). Zool. Sci. Contrib. N. Y. Zool. Soc. *50*, 1–39. https://doi.org/10.5962/p.206662.

101. Davies, N.B. (1978). Territorial defence in the speckled wood butterfly (*Pararge aegeria*): The resident always wins. Anim. Behav. *26*, 138–147. https://doi.org/10.1016/0003-3472(78)90013-1.

102. Horn, H.S. (2021). Social Butterflies (Princeton University Press). https://doi.org/10.2307/j.ctv1g13jwt.

103. Stutt, A.D., and Willmer, P. (1998). Territorial defence in speckled wood butterflies: do the hottest males always win? Anim. Behav. *55*, 1341–1347. https://doi.org/10.1006/anbe.1998.0728.

104. Wickman, P.-O., and Wiklund, C. (1983). Territorial defence and its seasonal decline in the speckled wood butterfly (*Pararge aegeria*). Anim. Behav. *31*, 1206–1216. https://doi.org/10.1016/S0003-3472(83)80027-X.

105. Lederhouse, R.C. (1982). Territorial defense and lek behavior of the black swallowtail butterfly, Papilio polyxenes. Behav. Ecol. Sociobiol. *10*, 109–118. https://doi.org/10.1007/BF00300170.

106. Pliske, T.E. (1975). Courtship Behavior of the Monarch Butterfly, Danaus plexippus L. Ann. Entomol. Soc. Am. *68*, 143–151. https://doi.org/10.1093/aesa/68.1.143.

107. Rutowski, R.L., Alcock, J., and Carey, M. (1989). Hilltopping in the Pipevine Swallowtail Butterfly (Battus philenor). Ethology *82*, 244–254. https://doi.org/10.1111/j.1439-0310.1989.tb00505.x.

108. Rutowski, R.L. (1977). The use of visual cues in sexual and species discrimination by males of the small sulphur butterflyEurema lisa (lepidoptera, pieridae). J. Comp. Physiol. *115*, 61–74. https://doi.org/10.1007/BF00667785.

109. Silberglied, R.E., and Taylor, O.R. (1978). Ultraviolet reflection and its behavioral role in the courtship of the sulfur butterflies Colias eurytheme and C. philodice (Lepidoptera, Pieridae). Behav. Ecol. Sociobiol. *3*, 203–243. https://doi.org/10.1007/BF00296311.

110. Crane, J. (1955). Imaginal behavior of a Trinidad butterfly, Heliconius erato hydara Hewitson, with special reference to the social use of color. Zool. Sci. Contrib. N. Y. Zool. Soc. *40*, 167–196. https://doi.org/10.5962/p.203427.

111. Rutowski, R.L. (1985). Evidence for Mate Choice in a Sulphur Butterfly (Colias eurytheme). Z. Tierpsychol. *70*, 103–114. https://doi.org/10.1111/j.1439-0310.1985.tb00504.x.

112. Bergman, M., Gotthard, K., Berger, D., Olofsson, M., Kemp, D.J., and Wiklund, C. (2007). Mating success of resident versus non-resident males in a territorial butterfly. Proc. Biol. Sci. *274*, 1659–1665. https://doi.org/10.1098/rspb.2007.0311.

113. Trischler, C., Kern, R., and Egelhaaf, M. (2010). Chasing behavior and optomotor following in free-flying male blowflies: Flight performance and interactions of the underlying control systems. Front. Behav. Neurosci. *4*, 20. https://doi.org/10.3389/fnbeh.2010.00020.

114. Egelhaaf, M. (1987). Dynamic properties of two control systems underlying visually guided turning in house-flies. J. Comp. Physiol. *161*, 777–783. https://doi.org/10.1007/BF00610219.

115. Duistermars, B.J., Reiser, M.B., Zhu, Y., and Frye, M.A. (2007). Dynamic properties of large-field and small-field optomotor flight responses in Drosophila. J. Comp. Physiol. A Neuroethol. Sens. Neural Behav. Physiol. *193*, 787–799. https://doi.org/10.1007/s00359-007-0233-y.

116. Arikawa, K. (2003). Spectral organization of the eye of a butterfly, Papilio. J. Comp. Physiol. A Neuroethol. Sens. Neural Behav. Physiol. *189*, 791–800. https://doi.org/10.1007/s00359-003-0454-7.

117. Stavenga, D.G., Kinoshita, M., Yang, E.C., and Arikawa, K. (2001). Retinal regionalization and heterogeneity of butterfly eyes. Naturwissenschaften *88*, 477–481. https://doi.org/10.1007/s001140100268.

118. Matsushita, A., Stewart, F., Ilić, M., Chen, P.-J., Wakita, D., Miyazaki, N., Murata, K., Kinoshita, M., Belušič, G., and Arikawa, K. (2022). Connectome of the lamina reveals the circuit for early color processing in the visual pathway of a butterfly. Curr. Biol. *32*, 2291–2299.e3. https://doi.org/10.1016/j.cub.2022.03.066.

119. Shimohigashi, M., and Tominaga, Y. (1991). Identificaton of UV, green and red receptors, and their projection to lamina in the cabbage butterfly, Pieris rapae. Cell Tissue Res. *263*, 49–59. https://doi.org/10.1007/BF00318399.

120. Shimohigashi, M., and Tominaga, Y. (1999). Synaptic organization in the lamina of the superposition eye of a skipper butterfly, Parnara guttata. J. Comp. Neurol. *408*, 107–124. https://doi.org/10.1002/(SICI)1096-9861(19990524)408:1<107::AID-CNE8>3.0.CO;2-#.

121. Pirih, P., Ilić, M., Meglič, A., and Belušič, G. (2022). Opponent processing in the retinal mosaic of nymphalid butterflies. Philos. Trans. R. Soc. Lond. B Biol. Sci. *377*, 20210275. https://doi.org/10.1098/rstb.2021.0275.

122. Swihart, S.L. (1970). The neural basis of colour vision in the butterfly, *Papilio troilus*. J. Insect Physiol. *16*, 1623–1636. https://doi.org/10.1016/0022-1910(70)90262-3.

123. Swihart, S.L. (1972). The neural basis of colour vision in the butterfly, *Heliconius erato*. J. Insect Physiol. *18*, 1015–1025. https://doi.org/10.1016/0022-1910(72)90038-8.

124. Kinoshita, M., and Stewart, F.J. (2022). Cortical-like colour-encoding neurons in the mushroom body of a butterfly. Curr. Biol. *32*, R114–R115. https://doi.org/10.1016/j.cub.2021.12.032.

125. Rusanen, J., Frolov, R., Weckström, M., Kinoshita, M., and Arikawa, K. (2018). Non-linear amplification of graded voltage signals in the first-order visual interneurons of the butterfly Papilio xuthus. J. Exp. Biol. *221*, jeb179085. https://doi.org/10.1242/jeb.179085.

126. Reichstein, T., von Euw, J., Parsons, J.A., and Rothschild, M. (1968). Heart Poisons in the Monarch Butterfly. Some Aposematic Butterflies Obtain Protection from Cardenolides Present in Their Food Plants. Science *161*, 861–866. https://doi.org/10.1126/science.161.3844.861.

127. Nishida, R. (2017). Chemical Ecology of Poisonous Butterflies: Model or Mimic? A Paradox of Sexual Dimorphisms in Müllerian Mimicry. In Diversity and Evolution of Butterfly Wing Patterns, T. Sekimura, and H.F. Nijhout, eds. (Springer), pp. 205–220. https://doi.org/10.1007/978-981-10-4956-9_11.

128. Davis, A.K., Chi, J., Bradley, C., and Altizer, S. (2012). The Redder the Better: Wing Color Predicts Flight Performance in Monarch Butterflies. PLOS One *7*, e41323. https://doi.org/10.1371/journal.pone.0041323.

129. Ilić, M., Chen, P.-J., Pirih, P., Meglič, A., Prevc, J., Yago, M., Belušič, G., and Arikawa, K. (2022). Simple and complex, sexually dimorphic retinal mosaic of fritillary butterflies. Philos. Trans. R. Soc. Lond. B Biol. Sci. *377*, 20210276. https://doi.org/10.1098/rstb.2021.0276.

130. McCulloch, K.J., Macias-Muñoz, A., Mortazavi, A., and Briscoe, A.D. (2022). Multiple Mechanisms of Photoreceptor Spectral Tuning in Heliconius Butterflies. Mol. Biol. Evol. *39*, msac067. https://doi.org/10.1093/molbev/msac067.

131. Belušič, G., Ilić, M., Meglič, A., and Pirih, P. (2021). Red-green opponency in the long visual fibre photoreceptors of brushfoot butterflies (Nymphalidae). Proc. Biol. Sci. *288*, 20211560. https://doi.org/10.1098/RSPB.2021.1560.

132. Bernard, G.D., and Remington, C.L. (1991). Color vision in Lycaena butterflies: spectral tuning of receptor arrays in relation to behavioral ecology. Proc. Natl. Acad. Sci. USA *88*, 2783–2787. https://doi.org/10.1073/pnas.88.7.2783.

133. Calbó, J., Pagès, D., and González, J.-A. (2005). Empirical studies of cloud effects on UV radiation: A review. Rev. Geophys. *43*. https://doi.org/10.1029/2004RG000155.

134. Judd, D.B., MacAdam, D.L., Wyszecki, G., Budde, H.W., Condit, H.R., Henderson, S.T., and Simonds, J.L. (1964). Spectral Distribution of Typical Daylight as a Function of Correlated Color Temperature. J. Opt. Soc. Am. *54*, 1031–1040. https://doi.org/10.1364/JOSA.54.001031.

135. Rutowski, R.L., Gislén, L., and Warrant, E.J. (2009). Visual acuity and sensitivity increase allometrically with body size in butterflies. Arthropod Struct. Dev. *38*, 91–100. https://doi.org/10.1016/j.asd.2008.08.003.

136. Rutowski, R.L., and Warrant, E.J. (2002). Visual field structure in the Empress Leilia, Asterocampa leilia (Lepidoptera, Nymphalidae): dimensions and regional variation in acuity. J. Comp. Physiol. A Neuroethol. Sens. Neural Behav. Physiol. *188*, 1–12. https://doi.org/10.1007/s00359-001-0273-7.

137. Mallet, J., and Joron, M. (1999). Evolution of Diversity in Warning Color and Mimicry: Polymorphisms, Shifting Balance, and Speciation. Annu. Rev. Ecol. Syst. *30*, 201–233. https://doi.org/10.1146/annurev.ecolsys.30.1.201.

138. Davis, A.K., Cope, N., Smith, A., and Solensky, M.J. (2007). Wing Color Predicts Future Mating Success in Male Monarch Butterflies. Ann. Entomol. Soc. Am. *100*, 339–344. https://doi.org/10.1603/0013-8746(2007)100[339:WCPFMS]2.0.CO;2.

139. Brower, P. (1963). The evolution of sex-limited mimicry in butterflies. Proceedings of the 16th International Congress of Zoology *4*, 173–179.

140. Magnus, D. (1950). Beobachtungen zur Balz und Eiablage des Kaisermantels Argynnis paphia L. (Lep., Nymphalidae). Z. Tierpsychol. *7*, 435–449. https://doi.org/10.1111/j.1439-0310.1950.tb01635.x.

141. Preiss, R., and Futschek, L. (1985). Flight stabilization by pheromone-enhanced optomotor responses. Naturwissenschaften *72*, 435–436. https://doi.org/10.1007/BF00404890.

142. Willis, M., and Mark, A. (1990). Pheromone-modulated optomotor response in male gypsy moths, Lymantria dispar L.: Upwind flight in a pheromone plume in different wind velocities. J. Comp. Physiol. A *167*. https://doi.org/10.1007/BF00192664.

143. Helmholtz, H. von (1867). Handbuch der Physiologischen Optik (Leopold Voss).

144. Komban, S.J., Alonso, J.-M., and Zaidi, Q. (2011). Darks Are Processed Faster Than Lights. J. Neurosci. *31*, 8654–8658. https://doi.org/10.1523/JNEUROSCI.0504-11.2011.

145. Kremkow, J., Jin, J., Komban, S.J., Wang, Y., Lashgari, R., Li, X., Jansen, M., Zaidi, Q., and Alonso, J.-M. (2014). Neuronal nonlinearity explains greater visual spatial resolution for darks than lights. Proc. Natl. Acad. Sci. USA *111*, 3170–3175. https://doi.org/10.1073/pnas.1310442111.

146. Pons, C., Mazade, R., Jin, J., Dul, M.W., Zaidi, Q., and Alonso, J.-M. (2017). Neuronal mechanisms underlying differences in spatial resolution between darks and lights in human vision. J. Vis. *17*, 5. https://doi.org/10.1167/17.14.5.

147. Braun, J., Hurtak, F., Wang-Chen, S., and Ramdya, P. (2024). Descending networks transform command signals into population motor control. Nature *630*, 686–694. https://doi.org/10.1038/s41586-024-07523-9.

148. Scherer, C., and Kolb, G. (1987). Behavioral experiments on the visual processing of color stimuli inPieris brassicae L. (Lepidoptera). J. Comp. Physiol. *160*, 645–656. https://doi.org/10.1007/BF00611937.

149. van der Kooi, C.J., and Kelber, A. (2022). Achromatic Cues Are Important for Flower Visibility to Hawkmoths and Other Insects. Front. Ecol. Evol. *10*, 819436. https://doi.org/10.3389/fevo.2022.819436.

150. Swihart, C.A., and Swihart, S.L. (1970). Colour selection and learned feeding preferences in the butterfly, Heliconius charitonius Linn. Anim. Behav. *18*, 60–64. https://doi.org/10.1016/0003-3472(70)90071-0.

151. Dyer, A.G., Boyd-Gerny, S., Shrestha, M., Lunau, K., Garcia, J.E., Koethe, S., and Wong, B.B.M. (2016). Innate colour preferences of the Australian native stingless bee Tetragonula carbonaria Sm. J. Comp. Physiol. A Neuroethol. Sens. Neural Behav. Physiol. *202*, 603–613. https://doi.org/10.1007/s00359-016-1101-4.

152. Goyret, J., Pfaff, M., Raguso, R.A., and Kelber, A. (2008). Why do Manduca sexta feed from white flowers? Innate and learnt colour preferences in a hawkmoth. Naturwissenschaften *95*, 569–576. https://doi.org/10.1007/s00114-008-0350-7.

153. An, L., Neimann, A., Eberling, E., Algora, H., Brings, S., and Lunau, K. (2018). The yellow specialist: dronefly Eristalis tenax prefers different yellow colours for landing and proboscis extension. J. Exp. Biol. *221*, jeb184788. https://doi.org/10.1242/jeb.184788.

154. Blackiston, D., Briscoe, A.D., and Weiss, M.R. (2011). Color vision and learning in the monarch butterfly, Danaus plexippus (Nymphalidae). J. Exp. Biol. *214*, 509–520. https://doi.org/10.1242/jeb.048728.

155. Buchner, E. (1984). Behavioural Analysis of Spatial Vision in Insects. In Photoreception and Vision in Invertebrates, M.A. Ali, ed. (Springer), pp. 561–621. https://doi.org/10.1007/978-1-4613-2743-1_16.

156. Eckert, H. (1971). Die spektrale Empfindlichkeit des Komplexauges von Musca (Bestimmung aus Messungen der optomotorischen reaktion). Kybernetik *9*, 145–156. https://doi.org/10.1007/BF00290480.

157. Scherer, C., and Kolb, G. (1987). The influence of color stimuli on visually controlled behavior inAglais urticae L. andPararge aegeria L. (Lepidoptera). J. Comp. Physiol. *161*, 891–898. https://doi.org/10.1007/BF00610230.

158. Bernard, G.D. (1983). Dark-processes following photoconversion of butterfly rhodopsins. Biophys. Struct. Mech. *9*, 277–286. https://doi.org/10.1007/BF00535663.
159. Briscoe, A.D., and Bernard, G.D. (2005). Eyeshine and spectral tuning of long wavelength-sensitive rhodopsins: no evidence for red-sensitive photoreceptors among five Nymphalini butterfly species. J. Exp. Biol. *208*, 687–696. https://doi.org/10.1242/jeb.01453.
160. Vasas, V., Hanley, D., Kevan, P.G., and Chittka, L. (2017). Multispectral images of flowers reveal the adaptive significance of using long-wavelength-sensitive receptors for edge detection in bees. J. Comp. Physiol. A Neuroethol. Sens. Neural Behav. Physiol. *203*, 301–311. https://doi.org/10.1007/s00359-017-1156-x.
161. Arikawa, K., and Uchiyama, H. (1996). Red receptors dominate the proximal tier of the retina in the butterfly Papilio xuthus. J. Comp. Physiol. A *178*, 55–61. https://doi.org/10.1007/BF00189590.
162. Stavenga, D.G., and Arikawa, K. (2011). Photoreceptor spectral sensitivities of the Small White butterfly Pieris rapae crucivora interpreted with optical modeling. J. Comp. Physiol. A Neuroethol. Sens. Neural Behav. Physiol. *197*, 373–385. https://doi.org/10.1007/s00359-010-0622-5.
163. Blake, A.J., Pirih, P., Qiu, X., Arikawa, K., and Gries, G. (2019). Compound eyes of the small white butterfly Pieris rapae have three distinct classes of red photoreceptors. J. Comp. Physiol. A Neuroethol. Sens. Neural Behav. Physiol. *205*, 553–565. https://doi.org/10.1007/s00359-019-01330-8.
164. Mota, T., Gronenberg, W., Giurfa, M., and Sandoz, J.-C. (2013). Chromatic Processing in the Anterior Optic Tubercle of the Honey Bee Brain. J. Neurosci. *33*, 4–16. https://doi.org/10.1523/JNEUROSCI.1412-12.2013.
165. Hardcastle, B.J., Omoto, J.J., Kandimalla, P., Nguyen, B.M., Keleş, M.F., Boyd, N.K., Hartenstein, V., and Frye, M.A. (2021). A visual pathway for skylight polarization processing in Drosophila. eLife *10*, e63225. https://doi.org/10.7554/eLife.63225.
166. Kleiner, M., Brainard, D., Pelli, D., Ingling, A., Murray, R., and Broussard, C. (2007). What's new in psychtoolbox-3. Perception *36*, 1–16.
167. Karashchuk, P., Rupp, K.L., Dickinson, E.S., Walling-Bell, S., Sanders, E., Azim, E., Brunton, B.W., and Tuthill, J.C. (2021). Anipose: A toolkit for robust markerless 3D pose estimation. Cell Rep. *36*, 109730. https://doi.org/10.1016/j.celrep.2021.109730.
168. Mathis, A., Mamidanna, P., Cury, K.M., Abe, T., Murthy, V.N., Mathis, M.W., and Bethge, M. (2018). DeepLabCut: markerless pose estimation of user-defined body parts with deep learning. Nat. Neurosci. *21*, 1281–1289. https://doi.org/10.1038/s41593-018-0209-y.
169. Supple, J.A., Varennes-Phillit, L., Gajjar-Reid, D., Cerkvenik, U., Belušič, G., and Krapp, H.G. (2022). Generating spatiotemporal patterns of linearly polarised light at high frame rates for insect vision research. J. Exp. Biol. *225*, jeb244087. https://doi.org/10.1242/jeb.244087.
170. O'Carroll, D. (1993). Feature-detecting neurons in dragonflies. Nature *362*, 541–543. https://doi.org/10.1038/362541a0.
171. Belušič, G., Ilić, M., Meglič, A., and Pirih, P. (2016). A fast multispectral light synthesiser based on LEDs and a diffraction grating. Sci. Rep. *6*, 32012. https://doi.org/10.1038/srep32012.
172. Kelber, A. (1999). Ovipositing butterflies use a red receptor to see green. J. Exp. Biol. *202*, 2619–2630. https://doi.org/10.1242/jeb.202.19.2619.
173. Backhaus, W., and Menzel, R. (1987). Color distance derived from a receptor model of color vision in the honeybee. Biol. Cybern. *55*, 321–331. https://doi.org/10.1007/BF02281978.
174. Laughlin, S. (1981). A Simple Coding Procedure Enhances a Neuron's Information Capacity. Z. Naturforsch. C Biosci. *36*, 910–912. https://doi.org/10.1515/znc-1981-9-1040.
175. Perry, M., Kinoshita, M., Saldi, G., Huo, L., Arikawa, K., and Desplan, C. (2016). Molecular logic behind the three-way stochastic choices that expand butterfly colour vision. Nature *535*, 280–284. https://doi.org/10.1038/nature18616.
176. Pirih, P., Meglič, A., Stavenga, D., Arikawa, K., and Belušič, G. (2020). The red admiral butterfly's living light sensors and signals. Faraday Discuss. *223*, 81–97. https://doi.org/10.1039/D0FD00075B.
177. Stavenga, D.G. (2002). Reflections on colourful ommatidia of butterfly eyes. J. Exp. Biol. *205*, 1077–1085. https://doi.org/10.1242/jeb.205.8.1077.
178. Cohen, M.X. (2023). Modern Statistics: Intuition, Math, Python, R (Independently published).
179. Cohen, M.X. (2014). Analyzing Neural Time Series Data: Theory and Practice (The MIT Press). https://doi.org/10.7551/mitpress/9609.001.0001.

STAR★METHODS

KEY RESOURCES TABLE

REAGENT or RESOURCE	SOURCE	IDENTIFIER
Deposited data		
Wing reflectance, photoreceptor spectral sensitivity, DN electrophysiology, and optomotor response data	Zenodo.org	Zenodo: https://doi.org/10.5281/zenodo.17604651
Matlab analysis code	GitHub.com	Github: https://github.com/jacksupple/Supple_2025_butterfly_spectral_tuning
Experimental models: Organisms/strains		
Danaus Plexippus	Stratford-upon-Avon Butterfly Farm Ltd, UK; The Entomologist, UK	RRID: NCBITaxon_13037
Myscelia cyaniris	Stratford-upon-Avon Butterfly Farm Ltd, UK; The Entomologist, UK	RRID: NCBITaxon_127357
Software and algorithms		
MATLAB 2021a	Mathworkds ltd.	RRID: SCR_001622; https://uk.mathworks.com/products/matlab.html
Spike 2	Cambridge Electronic Design, UK	RRID: SCR_000903; https://ced.co.uk/products/spkovin
Psychtoolbox 3.0	Kleiner et al.[166]	RRID: SCR_002881; http://psychtoolbox.org/
SpinView	Teledyne, Canada	https://www.teledynevisionsolutions.com/en-gb/products/spinnaker-sdk
Anipose	Karashchuk et al.[167]	RRID: SCR_023041; https://anipose.readthedocs.io/en/latest/
Deeplabcut 2.3	Mathis et al.[168]	RRID: SCR_021391; https://github.com/DeepLabCut/DeepLabCut
CIED65 standard daylight illuminant spectrum	International Commission on Illumination, Commission Internationale de l'Eclairage, CIE	ISO/CIE 11664-2:2022
Other		
Xenon short-arc bulb	Thorlabs, USA	Cat# SLS205
Flame USB spectrometer	Ocean Optics, USA	Cat# 9998FLM-002
Rear projection screen	Screen-Tech e.K., Hohenaspe, Germany	Model: ST-Pro-X
galvo scanner	Shenzhen City Aoxinjie Technology, China	Model: AT20L-L
Multi-LED LED-engin	ams-OSRAM, Austria	Cat# LZ7-04M100
5mm liquid light guide	Newport, USA	Cat# 77634
EF 100mm f/2.8L Macro IS USM lens	Canon, USA	Cat# 3554B002
Micro 1401 ADC	Cambridge Electronic Design, UK	RRID: SCR_018846; https://ced.co.uk/products/mic4in
DLP Lightcrafter 3010	Texas Instruments, USA	Model: DLPDLCR3010EVM
240 Hz LCD computer monitor	Samsung, South Korea	Model: S25BG400EU
Xe arc lamp OptoSource Illuminator	Cairn, UK	Model: XBO 75 W/2
2–3 MOhm tungsten electrodes	Microelectrodes Ltd., UK	Model: tungsten / 125um / 15–18um / unplated /220-P02 / 15mm https://microelectrodes.net/
3 MOhm FHC tungsten electrodes	FHC Ltd., USA	Model: UEWSHGSE3P1M
Extracellular Amplifier	Warner Instruments, USA	Model: DP-314
High-speed cameras	Teledyne, Canada	Model: BFS-U3-04S2M-CS
6mm UC Series Fixed Focal Length Lens	Edmund Optics, USA	Cat# 33-301
IR long-pass filter	Edmund Optics, USA	Cat# 12-766
Retro-reflective tape	Qualisys, Sweden	Cat# 160054

EXPERIMENTAL MODEL AND STUDY PARTICIPANT DETAILS

Animals

Monarch (*Danaus plexippus*; Subfamily: *Danainae*, Tribe: *Danaini*; RRID: NCBITaxon_13037) and Blue-Wave (*Myscelia cyaniris*; Subfamily: *Biblidinae*, Tribe: *Epicaliini*; RRID: NCBITaxon_127357) butterflies were purchased as pupae from Stratford Butterfly Farm (UK) and The Entomologist Ltd. (UK). Pupae were stored at 23°C and 60% humidity on a 12-hr dark/light cycle. Imagoes were allowed to harden for 24-hrs post-emergence, then stored at 15°C. Butterflies were fed diluted honey every other day, and all experiments were performed within two weeks post-emergence.

METHOD DETAILS

All experiments were performed at room temperature (23°C).

Wing reflectance measurements

Wings were amputated and flattened between two microscopy slides. The wing was illuminated by a Xenon short-arc bulb (SLS205, Thorlabs, USA) via a 200μm fibre and lens shutter which produced a ∼2mm diameter collimated light beam. Light was incident at an angle of 40° and measured using a calibrated Flame USB spectrometer (Cat#: 9998FLM-002, Ocean Optics, USA). Throughout this paper, ‘reflectance spectrum’ refers to the fraction of illuminant photon radiance reflected as a function of wavelength, and is assumed to be independent of the illuminant spectrum at the tested range of intensities. A ‘reflection spectrum’, in contrast, is defined as the spectrum of photon radiance reflected from the wing, which does depend on the illuminant spectrum. Under white light illumination, the normalised reflection spectrum corresponds to the normalised reflectance. Under any other illuminant, the reflection spectra is a function (assumed here as multiplication) of the reflectance and the illuminant spectrum. Natural reflection spectra were estimated by multiplying the standard wing reflectance with the CIED65 standard daylight illuminant spectrum (ISO/CIE 11664-2:2022; International Commission on Illumination, Commission Internationale de l’Eclairage, CIE).

Visual stimuli

For descending neuron electrophysiological experiments, butterflies were positioned with their head centred 12 cm from a 16 x 9 cm (width x height) rear projection screen (ST-Pro-X, Screen-Tech e.K., Hohenaspe, Germany), thereby subtending 67° x 41° (azimuth x elevation) of the frontal visual field. A customised display system comprising a multi-LED galvo scanner and an RGB DLP projector was focussed onto the rear surface of the projection screen (Figure S1).

The multi-LED galvo scanner AT20L-L (Shenzhen City Aoxinjie Technology, China) was illuminated by six LEDs (LED-Engin LZ7-04M100, ams-OSRAM, Austria; peak wavelengths: 395/450/499/518/595/636nm; Figure S1) transmitted via a 5 mm diameter liquid light guide (Newport, USA). The light guide output was focussed onto the rear surface of the projection screen via an EF 100mm f/2.8L Macro IS USM lens (Canon, Japan), generating an 8°-diameter circular bright target on a dark background. The horizontal and vertical position of the target was controlled by two orthogonal galvo-mounted mirrors (RGB-Lasers, Netherlands). Each galvo motor was controlled by a driver with ±10 V input. Voltages were generated in Spike2 software and output from a Micro 1401 ADC (CED, UK) at 1 kHz temporal resolution. Linear voltage ramps moved the bright target across the screen at 115 °/s. For each trajectory, the target first remained stationary at the start position for 500 ms to exclude transient responses to target appearance from the measurement. The color of the moving target was varied sequentially in ABBA sequence to mitigate time-dependent changes in the adaptation state of the neuron. LED emission intensities were measured using a calibrated spectrometer (Flame USB, Ocean Optics, USA). Linear regressions of the integrated LED spectra photon count vs input pulse-width modulation (PWM) were calculated and used to equalise the output of each LED to match the maximum output of the dimmest LED.

The RGB DLP projector (Lightcrafter 3010, Texas Instruments, USA) was used to present different sequences of moving targets (including variable size/velocity) and gratings to discern neuron types. Moving patterns were generated at 1280 x 720-pixel resolution in monochromatic mode with 8-bit depth to increase the native DLP framerate to 360 Hz. The intensities of each RGB LED were equalised by adjusting the supply current using the same calibration procedure as used for the LED-Engin (Figure S1). DLP Local Area Brightness Boost was enabled and set to strength and sharpness of 0, and Content Adaptive Illumination Control was disabled to ensure that the calibrated LED intensities were used. Moving patterns were generated in MATLAB using PsychToolBox,[166] rendering sequential patterns onto each RGB subframe to achieve 360 Hz frame rates.[169] Visual stimuli timings were aligned with electrophysiology via a photodiode measuring a small 100-pixel square in the corner of the screen which alternated on/off every frame.

DN units were classified using a sequence of standardised green visual stimuli presented in the frontal visual field using the DLP projector, comprising: (i) wide-field gratings moving sequentially in eight directions (10° spatial wavelength, 5 Hz temporal frequency, unless specified otherwise); (ii) rasterised scans of a small circular (4° diameter) dark target moving sequentially along eight directions to determine the spatial receptive field and preferred direction; (iii) square targets of varying size moving through the neuronal receptive field in the preferred direction. For receptive field mapping, the same 4°-diameter dark target stimulus was used for both WFDNs and TSDNs, and is similar to that used elsewhere.[59,62,170] Note that receptive fields were only measured in the frontal visual field region subtended by our stimulation screen, and receptive fields likely extend beyond the stimulated area. For size tuning, the targets moved at a constant velocity of 115°/s. For velocity tuning, the square target side lengths subtended 4°. Both target size and velocity tuning experiments presented each variable in ABBA sequence to mitigate time-dependent changes in the adaptation state of the neuron. For all moving target stimuli, the target appeared stationary at the start position for 150 ms prior to movement to exclude transient neuronal responses to target appearance. For color experiments, gratings were always either blue, green, or red bright bars presented on a black background. Note that for WFDN temporal frequency tuning curves, *Danaus* WFDNs were stimulated using the DLP display, whilst *Myscelia* data was collected on different animals at a later date using the same PC monitor used for optomotor experiments (below).

For optomotor experiments, butterflies were positioned with their head centred 10 cm from a 54 x 30 cm, 1920 x 1080 pixels (width x height) 240 Hz LCD computer monitor (S25BG400EU, Samsung, South Korea), thereby subtending 139° x 113° (azimuth x elevation) of the frontal visual field. Visual stimuli were generated at 240 Hz in MATLAB using PsychToolBox.[166] The intensity of each RGB color channel was equalised by adjusting the greyscale values, using the same linear regression calibration protocol as described for the LED-Engin. Moving gratings were presented sequentially for 2 seconds in both left and right directions with 20° spatial wavelength and temporal frequencies ranging from 0.1 Hz to 40 Hz. A small square trackbox in the corner of the screen turned white when stimuli were running to align the stimuli with stereo camera footage. An IR photodetector (Stock#: 642-4430, RS Components Ltd, UK) measured changes in trackbox intensity via an Arduino and was used to toggle an IR LED on/off within the stereo camera field of view.

Photoreceptor electrophysiology

Spectral sensitivity of the photoreceptors was measured with single-cell recordings of membrane potential during stimulation with iso-quantised flashes, produced with a Xe arc lamp (Cairn, UK) and a monochromator (B&M Optik, Germany) or with a multispectral LED array.[171] The method is described in detail elsewhere.[121,131] Photoreceptor identity was determined via angular maximum of polarization sensitivity (vertical for R1,2,9; horizontal for R3,4; diagonal for R5-8). For both species, animals of both sexes were surveyed. Each electrode excursion yielded many tens of impaled photoreceptors, which were quickly scanned with LED array. Finally, min. 4 cells per spectral class were scanned with the monochromator and included into the spectral sensitivity graph.

Descending neuron electrophysiology

Butterflies were mounted onto a large rotatable platform to position the screen in the frontal visual field of the butterfly (defined as parallel to the flat caudal surface of the butterfly head capsule). The ventral nerve cord was accessed ventrally, and a hypodermic needle fashioned into a hook supported the nerve during electrophysiological recordings. 3-MOhm sharp tungsten electrodes (Microelectrodes Ltd. UK, and UEWSHGSE3P1M, FHC Ltd, USA) were used to measure extracellular descending neuron action potentials, which were amplified at 10k gain with an extracellular amplifier (DP-314, Warner Instruments, USA) and digitised at 25 kHz using a Micro 1401 (CED, UK), and spike-sorted in Spike2 (CED, UK; Figures S1F–S1K).

Spike sorting is subject to false positives (spikes from different neurons assigned to the same spike-sorted unit), false negative (spikes belonging to the same neuron unassigned to the unit), and N-inflation (a single neuron counted as multiple units). False-positives were assessed from inter-spike interval histograms (with events less than 2ms classified as false positives, S1F-Kii). False positives and false negatives were assessed from time-continuous principal components of waveform shape (Figures S1F–S1K,iii–iv). To prevent N-inflation, most of our data report only one spike-sorted unit from a single recording. In those cases where multiple units are detected within the same recording, these units did not have the same receptive field/response properties. Given (i) the separation of waveform shapes, and (ii) differences in functional properties, we deduced these units to arise from distinct neurons. Furthermore, for each animal, only one instance of each cell type is reported. However, we did include bilaterally symmetric instances of the same cell type from the same animal (e.g. a cell sensitive to leftward optic flow in the left side of the cervical connective, and a cell sensitive to rightward optic flow in the right cervical connective). These units were always recorded from separate electrode penetrations from either the left or right side of the cervical connective.

Modelling DN responses from photoreceptor inputs

Photoreceptor responses were modelled following previous protocols.[160,172,173] Normalised photoreceptor voltage, V, was given by the log-logistic relation:

$$V = \frac{P^n}{P^n + 1}, \qquad \text{(Equation 1)}$$

where P (photon-catch) is the relative amount of light absorbed by each photoreceptor (normalised to the adapting background light level, below), and n is the Hill coefficient. Equation 1 therefore resembles the characteristic photoreceptor Voltage-log$_{10}$(Intensity) contrast-response function.[173] A Hill coefficient of 1 was used for all photoreceptors, corresponding to a dynamic range of ∼2 log units. Normalised photon-catch, P, was calculated as:

$$P = R \int_{300}^{700} S(\lambda) I_{LED}(\lambda) d\lambda, \qquad \text{(Equation 2)}$$

where λ is wavelength in nm, $S(\lambda)$ is the normalised photoreceptor spectral sensitivity, and $I_{LED}(\lambda)$ is the LED emission spectra (photons/cm^2/s). The range-sensitivity, R, scales the photon-catch dynamic range, and is modelled as the reciprocal photoreceptor photon-catch at the adapting background intensity, I_{BG} (photons/cm^2/s):

$$R = 1 \Big/ \int_{300}^{700} S(\lambda) I_{BG}(\lambda) d\lambda, \quad \text{(Equation 3)}$$

where R is formulated such that the adapting background photon radiance produces a normalised photoreceptor photon-catch of $P = 1$ from Equation 2, corresponding to a photoreceptor half-max response $V = 0.5$ from Equation 1, in accordance with the observation that photoreceptors maximise their information capacity by centring their dynamic range on the adapting background intensity.[173,174]

Photoreceptor responses were calculated for each of the six LEDs used for DN spectral tuning experiments. Best-fit photoreceptor weights were obtained by calculating a least-squares linear regression of the measured DN responses as a function of photoreceptor activation to the same LEDs, i.e.:

$$\min_{x} \|Ax - b\|^2, \quad \text{(Equation 4)}$$

where A is the matrix of photoreceptor responses to each LED (with dimensions: #LEDs x #photoreceptors), x is the vector of photoreceptor weights, and b is the vector of DN responses to each LED. Solution stability was assessed by comparing regularised fits with variable penalties for photoreceptor weight magnitudes, i.e.:

$$\min_{x} \left\{ \|Ax - b\|^2 + \alpha \|x\|^2 \right\}, \quad \text{(Equation 5)}$$

where α is the regularisation penalty weight.

Anatomical photoreceptor ratio estimates were based on measurements from simple/complex retinas in other species. In the simple retinal mosaic, the fractions of ommatidia UU:UB:BB are governed by two independent genetic switches in the photoreceptors R1 and R2.[175] Expression of the transcription factor Spineless in either photoreceptor results in the expression of blue opsin. With the Spineless expression probability p, q=(1-p), the ratio of UU:UB:BB is (q∧2):(2pq):(p∧2). In *Papilio xuthus*, p=1/2 and UU:UB:BB = 1:2:1.[175] In the more nymphaline *Vanessa atalanta*, the ommatidial ratio is UU:UB:BB = 4/9:4/9:1/9, therefore p=1/3.[176] Assuming a Spineless probability of p=1/3 and counting 6 green short visual fibers (i.e. R3-R8, assuming negligible R9 input), the final ratio of photoreceptor outputs for the simple mosaic is U:B:G = 2:1:9.

In the complex mosaic, the fraction of red (complex) ommatidia varies by species.[121,129,177] Following the distribution in the Nymphalid *Charaxes jasius* inferred from optical retinography,[121] the ratio of red:non-red ommatidia is ~1:3 (i.e. 25% red). For the non-red (simple) ommatidia, the ratio of U:B:G photoreceptors is 1:2:9 (corresponding to a Spineless probability of p~2/3). For red ommatidia, the relative ratio of U:B:G:$G^{+}R^{-}$:Y:R receptors equals approximately 1:2:6:3:12:3. Assuming an approximate ~1:2 ratio of red/non-red ommatidia,[121,129] this yields a combined relative retinal photoreceptor ratio of U:B:G:$G^{+}R^{-}$:Y:R = 1:2:8:1:4:1.

Head movements

Butterflies were tethered in front of a computer monitor in a dark arena by supergluing a 1 mm diameter steel rod to the mesoscutum and were encouraged to hold onto a small ~3x3 cm piece of tissue paper as a perch throughout the experiment. Head rotation was measured using two frame-synchronised FLIR Blackfly S USB3 0.4 Megapixel cameras (BFS-U3-04S2M-CS, Teledyne, Canada) recording at 250 frames per second using SpinView (Teledyne, Canada). Cameras were fitted with 6 mm fixed focal length lenses (UC Series, Edmund Optics, USA) with aperture set to f/5.6. To reduce luminance fluctuations from the visual stimulation, both lenses were fitted with an IR long-pass filter (25mm diameter, Stock #12-766, Edmund Optics, USA), and the butterfly was illuminated with IR LEDs (Model #S1120B, Splenssy). For *Danaus*, three natural circular head markings on the dorsal surface of the head capsule (vertex) were used to measure head orientation as they form a plane parallel to the transverse plane of the eye. In *Myscelia*, where natural head markings are absent, a small strip of retroreflective tape (Qualisys, Sweden) was mounted to the head to form the left-right lateral axis, and a small spot of white nail polish marked the rostral-caudal axis. Head markings were tracked using DeepLabCut.[168] Stereo-cameras were calibrated using a 7 x 6 checkerboard (side length = 3.126 mm), and stereo pairs of 2D xy pixel coordinates were triangulated into 3D xyz coordinates using Anipose.[167] Head orientation was calculated relative to the neutral head orientation, defined as the average across each ~5-minute recording. For each time point, the relative rotation matrix to align the local head coordinate system with the neutral head reference coordinate system was calculated using the dot product via the yaw-pitch-roll Tait–Bryan sequence. Head yaw-pitch-roll angles were subsequently smoothed using a Savitzky-Golay filter (3rd order, 404 ms window).

QUANTIFICATION AND STATISTICAL ANALYSIS

All data analysis was performed in MATLAB (The MathWorks, USA).

Descending neuron electrophysiology

For all DN tuning curves, responses were calculated as the average spike rate during pattern movement. DN receptive fields were calculated by extracting the position, and direction of target movement at the time of each spike. For each of the eight directions of target motion, pixels corresponding to the spike-triggered target location were transformed into visual azimuth/elevation, binned into a $5^o x 5^o$ grid, and smoothed using a gaussian kernel (1 standard deviation). Local motion sensitivity and preferred directions were calculated for each bin using the least-square sinusoidal fit of responses to each target direction. We did not include an estimate of neuronal latency when reconstructing DN receptive fields.

$WFDN_H$ spectral tuning curves were analysed using a one-way ANOVA, making the conservative assumption of independence between the six LED groups. Spectral tuning curves were normalised to the mean across LED conditions to remove variation in absolute spike rates between individuals. Statistically significant differences in the ANOVA results were further analysed by post-hoc t-test comparisons to the average response across LEDs.

Due to violations of normality and equality of variance, statistical analyses of DN tuning curves for gratings direction, temporal frequency, target size and velocity were performed using non-parametric permutation tests comparing the observed pairwise mean differences between color conditions to the empirical null distribution of pairwise differences, H_0[178,179] (Figures S2 and S3). For each animal, spike rate tuning curves were normalised by the min-max across color conditions. To generate H_0, pairwise differences were calculated from data pooled from the three color conditions across N animals, yielding $(3!)^N = 6^N$ unique pairwise mean differences. The probability of the observed mean differences occurring under H_0 (i.e., p-value) corresponds to the fraction of mean differences that are more extreme than the observed difference. To control for false positives from multiple testing across the independent variable range (i.e. gratings direction, target size, or target velocity, for which responses are correlated), H_0 was calculated separately and z-standardised for each variable, and the largest z-value across the independent variable for each permutation was stored to generate a max-value distribution. The 95th percentile of this max-value distribution was used as an adjusted significance threshold, and corrected p-values were calculated as the fraction of max-values more extreme than the observed mean differences (Figures S2 and S3). Finally, false positives from multiple testing across color conditions was controlled by applying the Bonferroni correction (three tests).

Head movements

Optomotor tuning curves were calculated by averaging the absolute change in head angle during moving gratings presentation. Temporal frequency tuning curves were calculated from the maximum average change in head angle per temporal frequency. Temporal frequency tuning curves were analysed by finding the maximum head angle across temporal frequencies per animal per color condition. Maximum head angle responses were non-normally distributed (Lilliefors goodness-of-fit, $p>0.05$), and therefore analysed using a repeated-measures Friedman test comparing color conditions, followed by pairwise t-test comparisons with Bonferroni correction.

Head movements to moving objects were normalised to the head orientation at the start of object movement. The maximum change in head yaw orientation towards the direction of target motion was pooled from all trials (Figure S4B). The 95th percentile of the cumulative distribution function (CDF) of maximum yaw values was used as a threshold to identify trials in which the animal tracked the object. Pair-wise differences between CDFs of yaw responses to different colors were analysed using two-sample Kolmogorov-Smirnov tests for each tested object size. P-values were adjusted with Bonferroni correction for color conditions.

Spectral alignment calculations

Spectral alignment between DN spectral tuning curves and (i) wing reflectance/reflections (Figure 5), and (ii) modelled photoreceptor combinations (Figures 2 and 5) was calculated as the Pearson correlation coefficient (i.e. cosine similarity) between 395-636nm (i.e., the range used to measure DN spectral tuning). For wing reflectance/reflection comparisons, TSDN spectral tuning curves were linearly interpolated and smoothed (Savitzky-Golay filter, 3rd order) with filter windows varying from 11 to 241 nm (Figures S5H–S5L).

Current Biology, Volume *36*

Supplemental Information

Species-specific spectral tuning of motion vision in butterflies

Jack A. Supple, Uroš Cerkvenik, Marko Ilić, Primož Pirih, Aleš Škorjanc, Gregor Belušič, and Holger G. Krapp

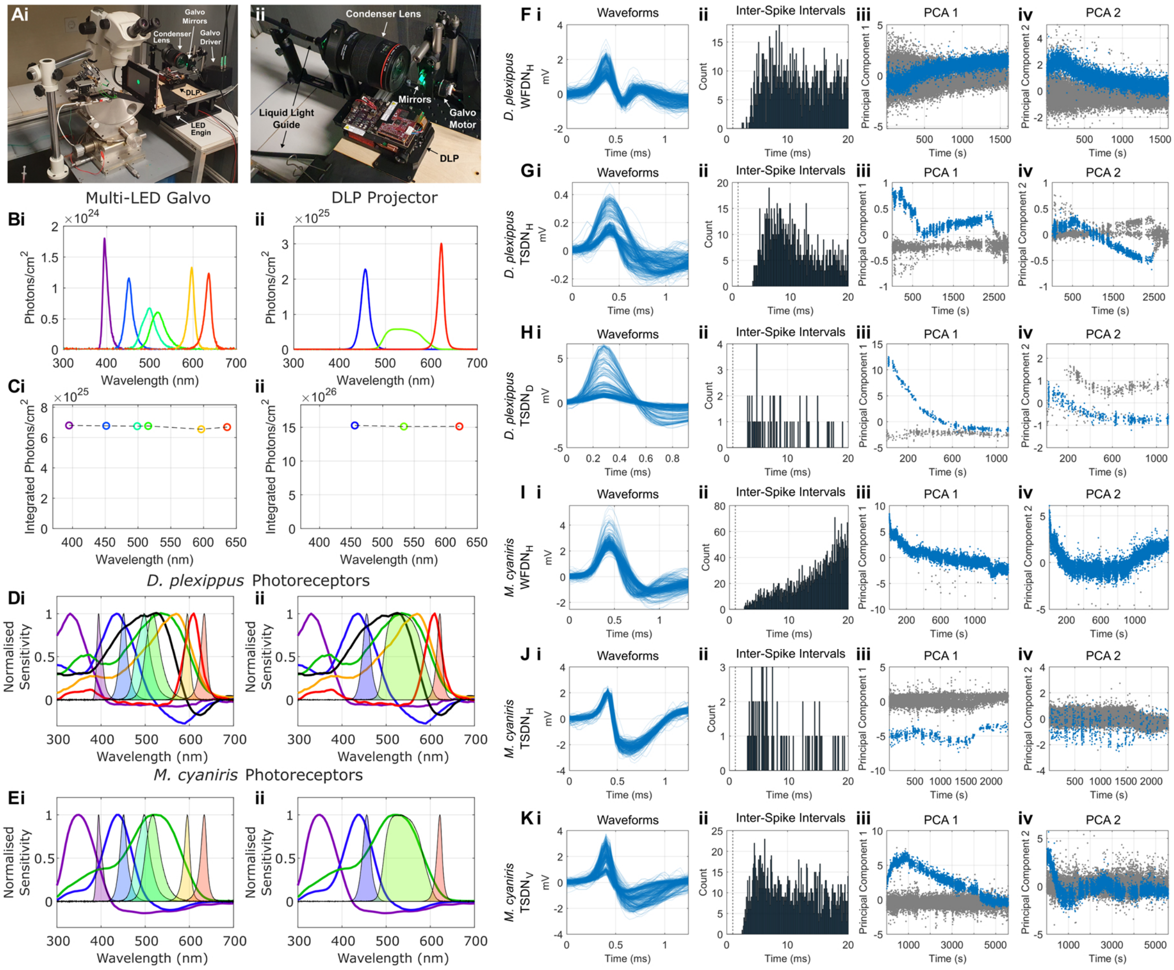

Figure S1. Multi-LED Galvo/DLP Calibration and Electrophysiological Spike Sorting. Related to Figures 2-3 & 5-6.

(A) Photographs of the electrophysiology set-up. (i) The butterfly is mounted on a rotation platform with the projection screen positioned in the frontal visual field. An example green target subtending 8°-diameter on the butterfly retina is presented from the multi-LED galvo system. (ii) Details of the display system. The galvo XY mirrors are in line with the DLP projection axis. A liquid light guide directs light from the LED Engin (out of view) into a Canon 100mm Macro lens acting as a condenser.

(B) Calibrated LED spectra for the (i) multi-LED galvo system, and (ii) the DLP projector.

(C) Integrated photon intensities for each calibrated LED.

(D) Normalised LED spectra with *D. plexippus* photoreceptors overlaid.

(E) Normalised LED spectra with *M. cyaniris* photoreceptors overlaid.

(F-K) Example spike-sorted DNs from (F-H) *D. plexippus*, and (I-K) *M. cyaniris*. (i) Random subset of 500 waveforms. (ii) Inter-spike interval histograms. Dashed line at 1ms. (iii) First principal component (PC1) of waveform shapes vs recording time. (iv) Second principal component (PC2) of waveform shapes vs recording time. Spike waveform shapes often drifted throughout recordings due to changes in electrode positioning and ventral nerve cord hydration; however, the same isolated unit could be identified due to the time-continuity of this drift in PC space.

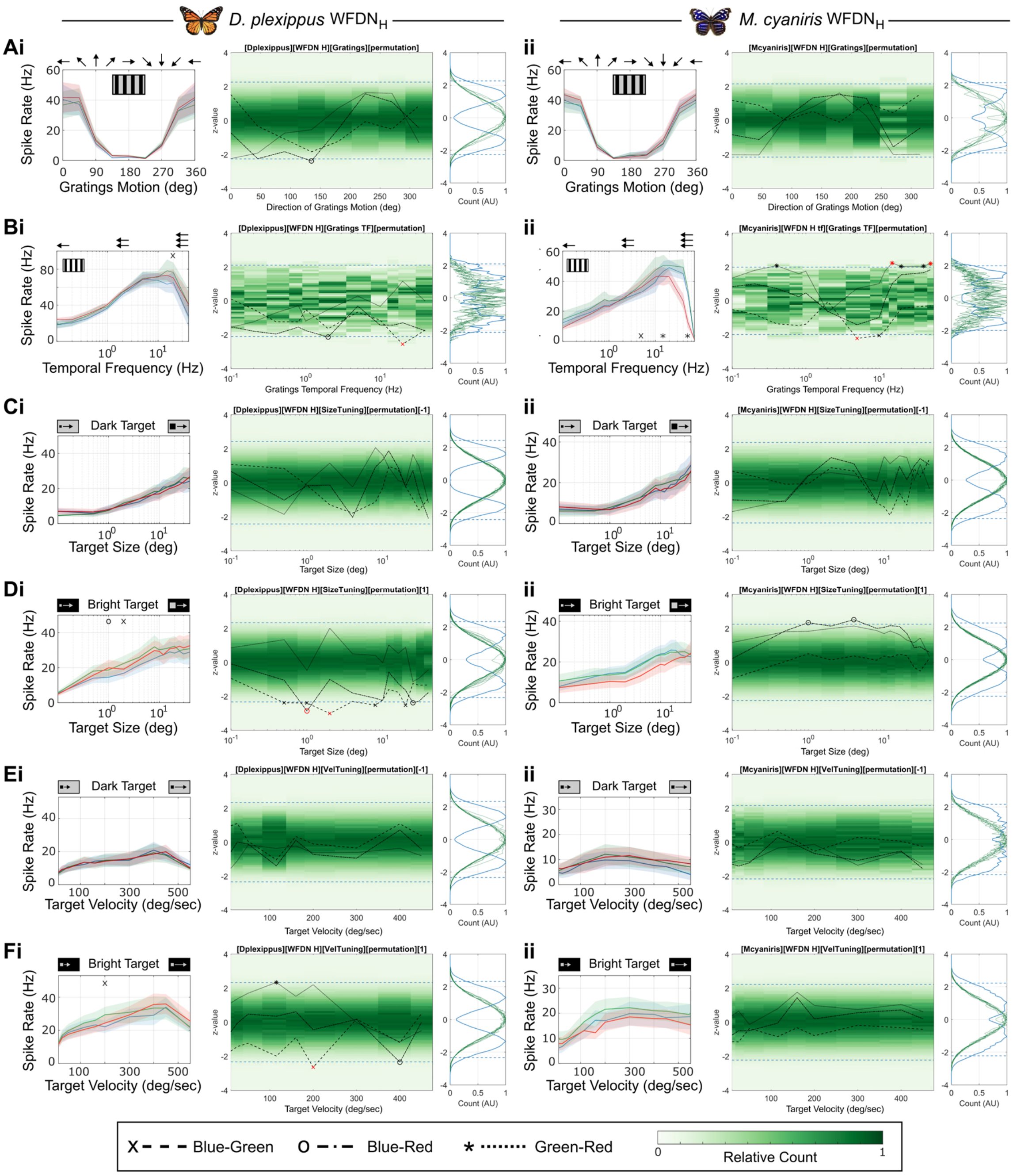

Figure S2. Non-Parametric Permutation Analysis of Butterfly WFDN Responses. Related to Figure 3. (Left panels) Tuning curves (reproduced from Figure 3) and **(middle-right panels)** permutation tests for **(i)** *D. plexippus*, and **(ii)** *M. cyaniris* WFDN$_H$ responding to **(A)** moving gratings; **(B)** moving gratings with different temporal frequencies, **(C)** dark targets and **(D)** bright targets of different size; **(E)** dark targets and **(F)** bright targets of different velocities. Note that only velocities ≤450°/sec were included in permutation analyses as not all animals were tested with higher velocities. **Middle panel** shows the z-standardised empirical null distribution H_0 (green) for each independent variable value (i.e. gratings direction, temporal frequency, target size, or target velocity). **Right panel** shows the same z-standardised H_0 distributions overlaid (green lines). The symmetric distribution in blue shows the histogram of maximum absolute difference values that occurred in each permutation. The significance threshold (dashed blue lines) controls for the family-wise error rate across the (correlated) independent variable, and corresponds to the 95th-percentile of the blue max-distribution. The observed pairwise firing rate differences between the three color conditions are plotted over H_0 in the middle panel (dash: blue-green; dot-dash: blue-red; dots: green-red). Black symbols ('x': blue-green; 'o': blue-red; '*': green-red) plotted beyond the max-value threshold (dashed blue) indicate observations that have a $p \leq 0.05$ of occurring were there no difference between responses to different colors, after correcting for multiple comparisons across the correlated independent variable. Red symbols indicate data that remains $p \leq 0.05$ after Bonferroni correction for multiple pair-wise comparisons across color conditions and correspond to the symbols in the tuning curves (left panel). See methods for additional details.

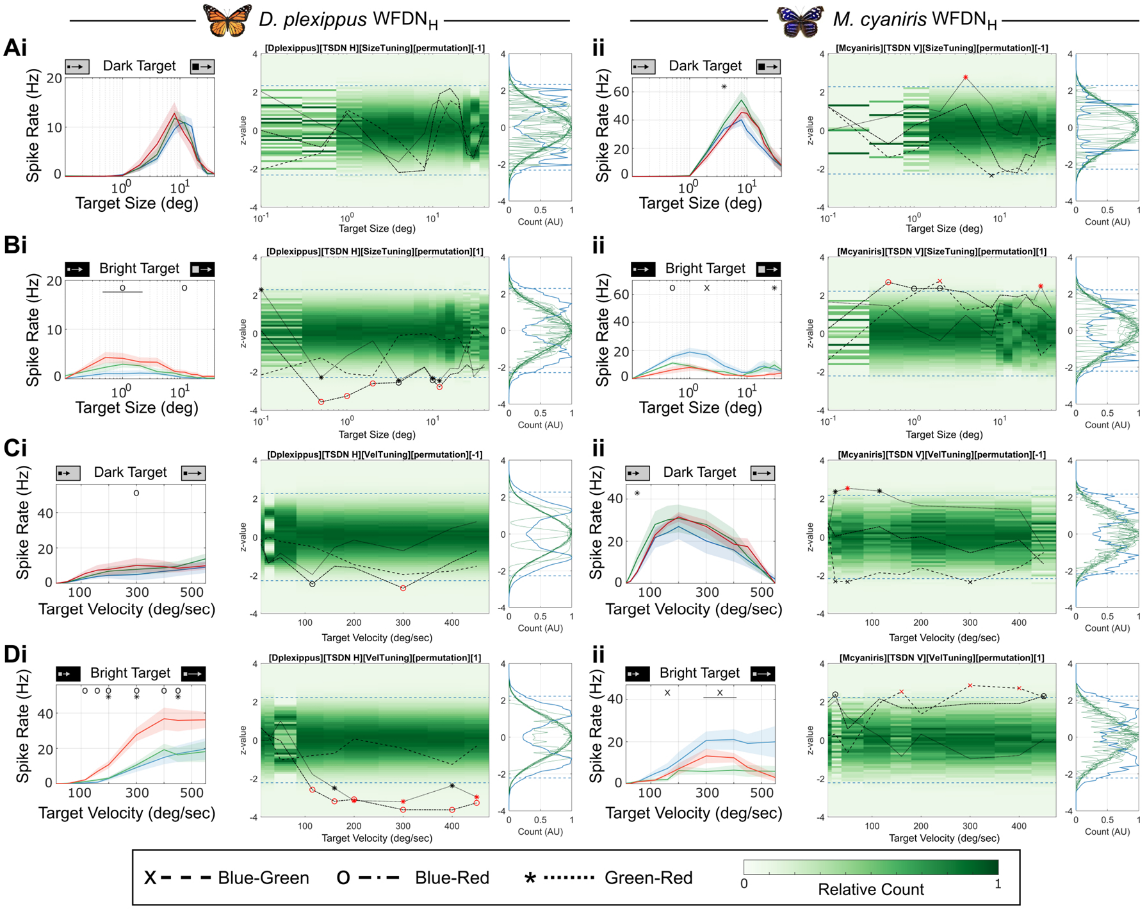

Figure S3. Non-Parametric Permutation Analysis of Butterfly TSDN Responses. Related to Figure 6. **(Left)** Tuning curves (reproduced from Figure 5) and **(middle-right panels)** permutation tests for **(i)** *D. plexippus* TSDN_H, and **(ii)** *M. cyaniris* TSDN_V responding to **(A)** dark targets and **(B)** bright targets of different size, and **(C)** dark targets and **(D)** bright targets of different velocities. Note that only velocities ≤450°/sec were included in permutation analyses as not all animals were tested with higher velocities. See Figure S2 for detailed panel descriptions.

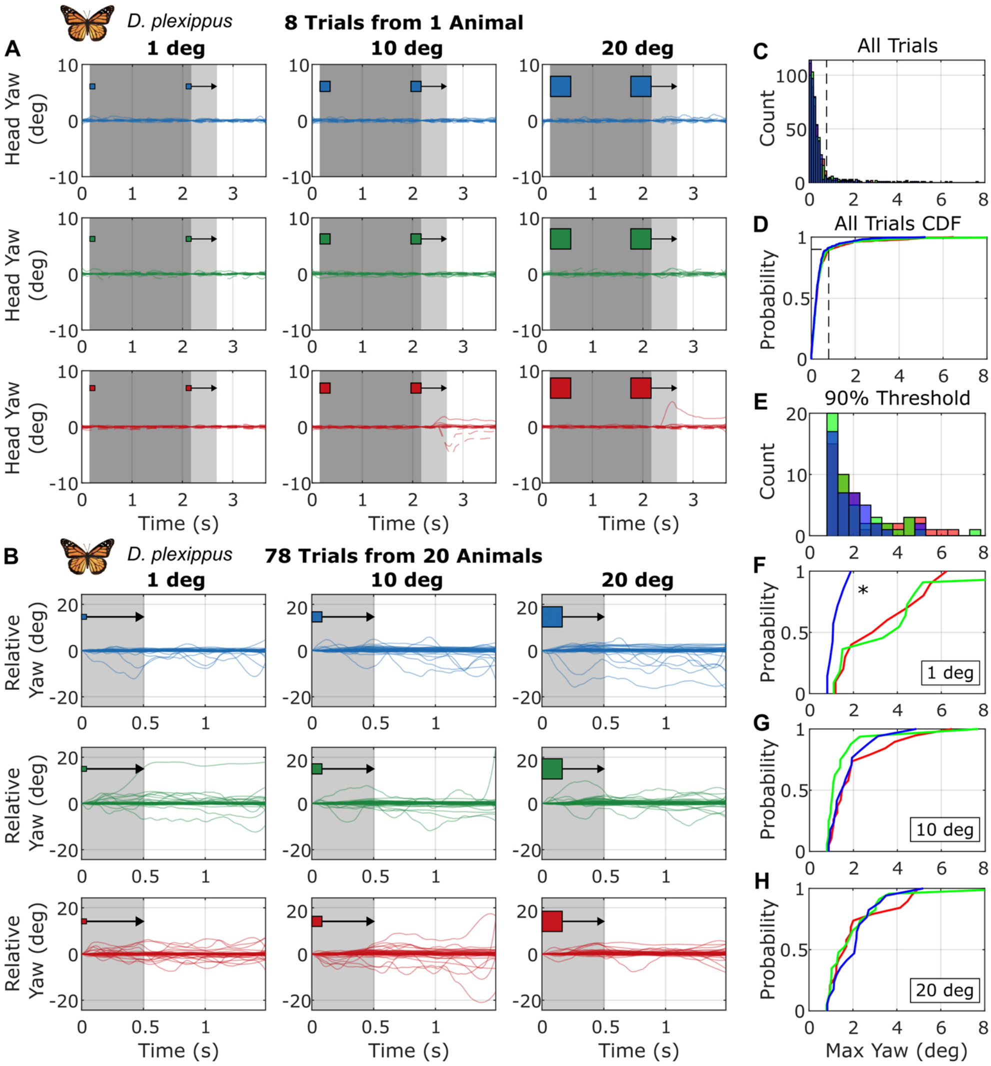

Figure S4. *D. plexippus* Head Movements to Moving Targets. Related to Figure 4.

(A) Example *D. plexippus* head yaw movements to horizontally moving targets of varying size (columns) and color (rows top/middle/bottom = blue/green/red). In each trial, a square target appears at one side of the screen and remains stationary for 2 seconds (dark grey area). The object then moves horizontally at 400°/sec (light grey area). Solid and dashed colored lines indicate responses to targets moving left and right, respectively.

(B) Combined trials from 20 animals, only showing periods of target movement (light grey area). Head angles are normalised to the position at the onset of target movement. Responses to leftward targets are flipped, so all movements towards the direction of object motion are positive.

(C) Histogram of maximum relative yaw angles (degrees) during the period of target movement in (B). Note subplots C-H share the same x-axis.

(D) Cumulative Distribution Function (CDF) of maximum yaw angles for all blue/green/red target trials. The 90th percentile is calculated and used as a threshold in plots (E-H).

(E) Histogram of maximum relative yaw angles (degrees), excluding trials with amplitudes less that the 90th percentile threshold.

(F-H) CDFs of thresholded yaw amplitudes for blue/green/red targets with diameters of (F) 1°, (G) 10°, and (H) 20°. Asterisk indicates statistically significant differences between blue-green (pairwise Kolmogorov–Smirnov test, p=0.034) and blue-red (p=0.017) 1° diameter targets, without correcting for multiple comparisons. Differences were no longer statistically significant (p>0.05) after Bonferroni correction.

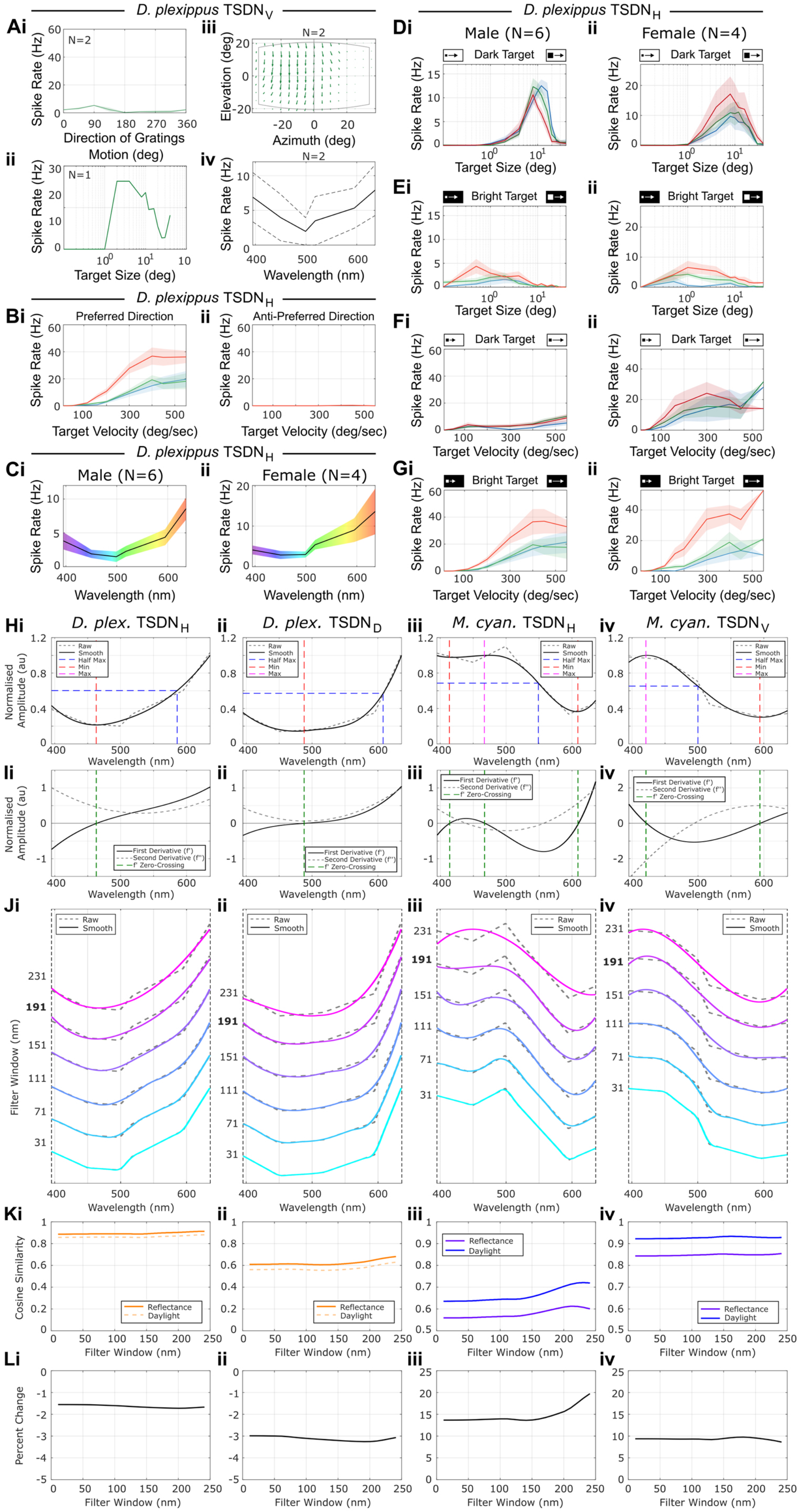
D. plexippus TSDN$_V$
Ai
N=2
Spike Rate (Hz)
Direction of Gratings Motion (deg)
0 90 180 270 360
iii
N=2
Elevation (deg)
Azimuth (deg)
-20 0 20
ii
N=1
Target Size (deg)
iv
N=2
Wavelength (nm)
400 500 600
D. plexippus TSDN$_H$
Bi
Preferred Direction
ii
Anti-Preferred Direction
Target Velocity (deg/sec)
100 300 500
D. plexippus TSDN$_H$
Ci
Male (N=6)
ii
Female (N=4)
Wavelength (nm)
D. plexippus TSDN$_H$
Di
Male (N=6)
ii
Female (N=4)
Dark Target
Target Size (deg)
Ei
Bright Target
Fi
Dark Target
Target Velocity (deg/sec)
Gi
Bright Target
Hi
D. plex. TSDN$_H$
ii
D. plex. TSDN$_D$
iii
M. cyan. TSDN$_H$
iv
M. cyan. TSDN$_V$
Raw
Smooth
Half Max
Min
Max
Normalised Amplitude (au)
Wavelength (nm)
Ii
First Derivative (f')
Second Derivative (f'')
f' Zero-Crossing
Ji
Raw
Smooth
Filter Window (nm)
231
191
151
111
71
31
Ki
Cosine Similarity
Reflectance
Daylight
Filter Window (nm)
0 50 100 150 200 250
Li
Percent Change
Filter Window (nm)

Figure S5. Additional TSDN Data, Parameterisation, and Smoothing. Related to Figures 5-7.
(A) *D. plexippus* $TSDN_V$ responses to (i) moving gratings (n=2), (ii) square dark targets of different sizes moving in the preferred direction (n=1), (iii) receptive field (n=2), and (ii) spectral tuning (n=2, individuals in dashed black, average in solid black). Stimulus parameters the same as Figure 5.
(B) *D. plexippus* $TSDN_H$ responses to bright square 4° (side-length) targets moving in the (i) preferred and (ii) anti-preferred direction (N=5 units from 4 animals). Panel (i) is reproduction of Figure 6Bii for comparison. Only responses to bright red objects shown in (ii). All plots show mean ± SEM.
(C-G) Comparison of *D. plexippus* $TSDN_H$ responses in (i) male (N=6 animals) and (ii) female (N=4 animals). **(C)** spectral tuning, **(D)** dark target size tuning, **(E)** bright target size tuning, **(F)** dark target velocity tuning, (G) bright target velocity tuning.
(H) TSDN spectral tuning raw data (dashed grey), smoothed data (solid black, filter window 191 nm), minima (dashed red), maxima (dashed magenta), and half-max (dashed blue). **(I)** Spectral tuning first and second derivatives (solid black, dashed grey), and first derivative zero crossings (dashed green). **(J)** Comparison of raw TSDN data (dashed grey) with smoothened TSDN spectral tuning (solid colors) using different filter window sizes. Filter window of 191 used for all calculations. **(K)** Cosine similarity between TSDN spectral tuning and wing reflectance (solid line) and daylight reflection (dashed line) for different smoothing window sizes. **(L)** Percent difference in cosine similarities between TSDN*Reflectance and TSDN*Daylight.